

ABSTRACT

RACHEL MARIE KING. On the Use of Wing Adaptation and Formation Flight for Improved Aerodynamic Efficiency. (Under the direction of Dr. Ashok Gopalaram.)

There is a continuous effort to improve the performance and efficiency of today's aircraft, and the reduction of aircraft drag has been the primary focus of many aerodynamicists. In the current research, two different and innovative approaches for aircraft drag reduction are examined. These approaches are: (1) multiple spanwise trailing-edge flaps, and (2) formation and ground-effect flight. The main goal of this dissertation was to assess the drag benefits of the two approaches, in an effort to explore their potential for use on future aircraft.

The first approach of using multiple trailing-edge flaps has the potential for application on aircraft in the near future. By using multiple trailing-edge flaps along the wing span, it is possible to redistribute the spanwise lift distribution to suit the flight condition. For this research, a numerical approach was developed for determining optimum lift distributions on a wing with multiple trailing-edge flaps for various flight conditions. The objective of the approach was to determine the flap angles that will reduce the drag at 1- g flight conditions, and constrain the wing root-bending moment at high- g conditions to not exceed a specified value. The approach uses the concept of additional and basic lift distributions, and the proper use of a trailing-edge flap for redistributing the aerodynamic loads to bring about a minimum in profile and induced drag. The results for the flap-angle distributions are presented for a planar and a nonplanar wing, along with post-design analysis and aircraft performance simulations used to validate the optimum flap-angle distributions determined using the numerical approach. It is shown that the approach is effective in determining optimum flap angles for reducing both profile and induced drag over a wide range of flight conditions. Performance benefits due to using the optimum flap angles are shown when compared to the zero-flap case. In addition, the trailing-edge flaps were found to be successful in relieving the wing root-bending moment at high- g flight conditions, which can be used to reduce wing weight.

When examining formation and ground-effect flight as another approach for

aircraft drag reduction, an optimum-downwash approach using a vortex-lattice implementation was used to study formations of wings loaded optimally for minimum induced drag with roll trim. An exact approach was also developed to examine the drag of elliptically-loaded wings in formation. The exact approach allows for decomposition of the benefits by considering the mutual-interference contributions from different pairs of wings in a formation. The results show that elliptically-loaded wing formations have nearly the same drag as optimally-loaded wing formations. For a formation of planar wings, in or out of ground effect, the optimum lateral separation corresponds to a 9%-span overlap of wing tips. At this optimum lateral separation, a formation of 25 elliptically-loaded wings flying out of ground effect experiences an 81% drag reduction compared to 25 wings flying in isolation. For large formations, in or out of ground effect, multiple local optima are seen for the lateral separation. Large formations experience small additional benefits due to ground effect even at relatively large ground clearances of four wing spans. The shape of vee-formations, for equipartition of drag benefits, is found to be nearly independent of flight in or out of ground effect.

Overall, both approaches for aircraft drag reduction show potential for significant drag savings. It is believed that the presented research will further increase interest in such flight techniques, and thus advance their progression toward becoming viable solutions for drag reduction on future aircraft.

On the Use of Wing Adaptation and Formation Flight for Improved Aerodynamic Efficiency

by

Rachel Marie King

A dissertation submitted to the Graduate Faculty of
North Carolina State University
in partial fulfillment of the
requirements for the Degree of
Doctor of Philosophy

Aerospace Engineering

Raleigh, NC
2005

APPROVED BY:

Dr. Ashok Gopalarathnam
Advisory Committee Chairman

Dr. Hassan A. Hassan
Advisory Committee Member

Dr. Jack R. Edwards
Advisory Committee Member

Dr. Xiao-Biao Lin
Advisory Committee Minor Rep.

Dedicated to the memory of my grandfather, Hugh Leo Marion.

BIOGRAPHY

Rachel Marie King was born on February 4, 1977 in Winston-Salem, NC, to Harry and Susan King. She attended North Forsyth High School in Winston-Salem, where she first decided to pursue a career in aerospace engineering. She graduated in 1995 and started attending North Carolina State University that fall. She graduated cum laude with a BS in Aerospace Engineering in May 1999. Upon graduation, she joined the graduate school at North Carolina State University as a research assistant for Dr. Ndaona Chokani. She obtained her MS in Aerospace Engineering in August 2001, studying the use of an adaptive mechanical turbulator for the control of laminar separation bubbles. In the summer of 2001, she attended Politecnico di Torino, in Turin, Italy, as a participant in the International Masters Program In Aerospace Engineering (IMSAE). While there, she studied flow control downstream of a backward facing step in a water tunnel using Digital Particle Image Velocimetry (DPIV).

In January 2003, Rachel joined the applied aerodynamics group at North Carolina State University to pursue her doctorate degree under the advisement of Dr. Ashok Gopalarathnam. Since then, her studies have focused on different approaches for aircraft drag reduction, including formation flight and the adaptive wing, resulting in two AIAA conference papers and an article to appear in *Journal of Aircraft*. After graduation, Rachel plans to move to the D.C. area to pursue employment in the field of experimental/applied aerodynamics.

ACKNOWLEDGEMENTS

I would first like to thank my advisor, Dr. Ashok Gopalarathnam, for his steadfast support and unlimited patience with me. He has taught me, and in some cases, re-taught me many things, and I appreciate, as well as admire, his dedication to his graduate students and his relentless pursuit for those hard-to-find answers to the problems we often encountered over the course of our research. I may not have been an exemplary graduate student at all times, but he has taught and inspired me to continue striving toward becoming the best researcher that I can be.

I would like to thank Dr. Hassan Hassan, Dr. Jack Edwards, and Dr. Xiao-Biao Lin for serving as my graduate committee members. I would also like to thank Dr. Peter B. S. Lissaman and Dr. John H. McMasters for valuable discussions regarding my research. Both of them have been more than generous in providing helpful advice and support, and for that I am honored.

In addition, I would like to thank my family for their endless love and support. In particular, I thank my father, Harry King, who never doubted that I could get this far. He has been my source of strength, and I would not be where I am today without his guidance. I also thank my grandparents, Hugh and Marie Marion. My grandfather looked forward to this moment as much as me, if not more, and although he is not here now to share it with me, I dedicate this dissertation to him in his memory.

And last but not least, I would like to thank Joe Norris. Although we have had to live far apart as I pursued my doctorate, he has always been available to listen and provide his love, support, and encouragement, for which I will always be grateful.

Table of Contents

List of Tables	vii
List of Figures	viii
Nomenclature	x
Chapter 1 Introduction	1
1.1 Multiple Spanwise Trailing-Edge Flaps	2
1.2 Formation and Ground-Effect Flight	5
1.3 Outline of Dissertation	8
Chapter 2 Ideal Lift Distributions and Flap Angles for Adaptive	
Wings	9
2.1 Background	10
2.1.1 Minimum Induced Drag with and without Root-Bending	
Moment Constraint	10
2.1.2 Minimum Profile Drag	17
2.1.3 Basic and Additional Lift Distributions	19
2.2 Methodology	22
2.2.1 Flap Angles for Minimum Drag	23
2.2.2 Flap Angles for Minimum Drag with a RBM Constraint	24
2.3 Results	25

2.3.1	Example 1: Planar Wing	25
2.3.2	Example 2: Nonplanar Wing	34
2.4	Summary	36
 Chapter 3 Ideal Aerodynamics of Ground-Effect and Formation		
	Flight	37
3.1	Methodology	38
3.1.1	Optimum Lift Distribution for Minimum Induced Drag . .	38
3.1.2	Ground Effect	45
3.1.3	Prescribed Elliptical Lift Distribution	46
3.1.4	Optimum Vee-Formation Shape	53
3.2	Validation of Optimum-Loading Method	55
3.2.1	Planar Wing Out of Ground Effect	55
3.2.2	Single Wing in Ground Effect	57
3.3	Results	60
3.3.1	Effect of Lateral Separation	60
3.3.2	Combined Formation and Ground-Effect Flight	64
3.3.3	Optimal Vee-Formation Shapes	72
3.4	Summary	74
 Chapter 4 Concluding Remarks 76		
 Chapter 5 Future Work 80		
 Chapter 6 References 82		
 Appendix A Modeling of Lateral Symmetry and Ground Reflec-		
	tions	90

List of Tables

2.1	Assumed geometry, drag, and power characteristics for the hypothetical general aviation airplane for Example 1.	26
-----	---	----

List of Figures

1.1	Multiple trailing-edge flaps on a swept wing.	3
2.1	Spanwise load curve on a nonplanar wing with three elements of variation.	11
2.2	Single symmetric wing with different RBM constraints: (a) Trefftz-plane downwash distributions, and (b) nondimensionalized spanload distributions.	16
2.3	Location of leading-edge stagnation point on an airfoil.	18
2.4	Lift distribution for wing with winglet, (a) additional and basic lift and (b) C_l due to superposition in comparison to C_l from WINGS. Inset in (b) shows rear view of nonplanar wing with five flaps. . .	21
2.5	Wing and tail geometry for Example 1.	26
2.6	Airfoil for Example 1: (a) geometry and velocity distribution, and (b) drag polar at $Re\sqrt{C_l} = 3 \times 10^6$	27
2.7	Spanwise C_l distributions and drag polars for flaps optimized for $C_L = 0.1, 0.5$, and 0.9	28
2.8	Spanwise C_l distributions and drag polars for the non-adapted wing (all flaps set to zero deg).	29
2.9	Spanwise Γ distributions for $C_L = 0.1, 0.5$, and 0.9 , for the adapted and non-adapted wings compared with the elliptical loading. . . .	30
2.10	Drag polars for zero flaps, and flaps optimized for $C_L = 0.1, 0.5$, and 0.9	31
2.11	Examination of performance benefits: (a) maximum velocity, (b) range, and (c) endurance.	32
2.12	Calculated C_l distributions for $C_L = 0.5$: (i) optimal distribution with no RBM constraint, (ii) optimal distribution with RBM constraint, iii) distribution calculated by WINGS with optimized flap angles.	33
2.13	Wing and winglet geometry for Example 2.	34
2.14	Spanwise C_l distributions and drag polars for flaps optimized for $C_L = 0.5$	35
3.1	Illustration of the loading and Trefftz-plane normalwash for the two-wing example.	39
3.2	Illustration of vortex-lattice arrangement for a pair of swept wings.	41

3.3	Model of two-wing formation in ground effect.	46
3.4	Variation with y/b for various z/b of the downwash in the Trefftz plane for an elliptically-loaded wing. Inset shows wake trace and coordinate system.	48
3.5	A pair of elliptically loaded wings, A and B: (a) illustration of the wake-trace geometry, with the streamlines shown for wing A, and (b) contours of D_{int}/D_{ell} as a function of Y_2/b and Z_2/b	50
3.6	Numbering for a seven-wing vee formation.	54
3.7	Comparison of the optimal solution for a planar wing from VLM with the exact solution: (a) spanload distribution and (b) convergence of the predicted induced drag with increasing number of lattices per half span.	56
3.8	Comparison of drag factors for wings in ground effect from the current method with exact solutions from Ashill.	58
3.9	Planar and nonplanar wings in ground effect at various h : (a) Trefftz-plane downwash distributions for planar wings, (b) spanload distributions for planar wings, (c) Trefftz-plane normalwash distributions for nonplanar wings, and (d) spanload distributions for nonplanar wings.	59
3.10	Two-wing formation: (a) variation of the formation drag ratio with lateral separation for optimal and elliptical loadings, with insets showing the wake traces, and (b) comparison of the superposed loading with the “best” loading for $Y/b = 1$ and $Y/b = 0.91$	62
3.11	Wing formation in ground effect: (a) optimum Trefftz-plane downwash distributions and (b) optimum spanload distributions at various h	66
3.12	Exact results for the effect of lateral separation on drag ratio for three- and 25-wing formations in and out of ground effect with insets showing the plan views of formation geometries at arbitrary streamwise spacings.	68
3.13	Drag ratios for a single wing and for formations of three and 25 wings in ground effect.	70
3.14	A 25-wing formation in and out of ground effect ($h/b = 1.0$): (a) optimum vee-formation shape, and (b) gradient of individual induced drag with streamwise location.	73
A.1	Single wing with lateral symmetry, with vorticity distribution modeled with four horseshoe vortices.	91
A.2	Two-wing formation in ground effect, with each wing modeled with a single horseshoe vortex.	93

Nomenclature

A, B constants used in defining normalwash distribution

A_0, A_1 coefficients of Fourier series

b wing span

b_{eff} effective formation span

c local chord

C_D wing drag coefficient

C_{dp} section profile drag coefficient

C_L wing lift coefficient

C_l section lift coefficient

C_{la} additional lift coefficient

C_{lb} basic lift coefficient

C_{RBM} wing root-bending moment coefficient

D induced drag

D_{ell} induced drag of a single elliptically-loading wing out of ground effect

D_{ff} interference drag due to formation flight

D_{ge}	interference drag due to ground proximity
D_{int}	mutual-interference drag for a pair of wings
\mathbf{F}	residual vector
f	index of the term for formation-flight interference drag
g	index of the term for ground-effect interference drag
h	height of wing above ground
\mathbf{I}	influence coefficient matrix of size $n \times n$
\mathbf{J}	Jacobian matrix
L	wing lift
l	winglet height
L'_a	additional loading
L'_b	basic loading
m	number of trailing-edge flaps
N	number of wings
n	number of horseshoe vortices
P, Q	constants used in defining normalwash distribution
q	function defining contribution of unit load to wing root-bending moment, Eq. 2.3
R	wing rolling moment
r	function defining contribution of unit load to wing rolling moment, Eq. 3.3

Re	Reynolds number
RBM	wing root-bending moment
S	wing surface area
s	arc length along a wake trace of a wing
V_∞	freestream velocity
V_{max}	level-flight maximum speed
\overline{w}	normalwash at quarter-chord
W	cross-flow velocity distribution in the Trefftz-plane
w	normalwash/downwash in the Trefftz-plane
\mathbf{w}	vector containing the n Trefftz-plane normalwash values
w_0	Trefftz-plane downwash at mid-span location on wing wake trace
X	streamwise separation between adjacent wings
x	streamwise coordinate
x_f	chordwise location of flap hinge
Y	centerline-to-centerline lateral separation between adjacent wings
y	spanwise coordinate
\mathcal{Z}	complex coordinate in the Trefftz plane
Z	vertical separation between adjacent wings
z	vertical coordinate

α	wing angle of attack
δ_f	flap deflection angle
$\hat{\delta}_f$	flap-angle distribution about the mean flap deflection angle
$\bar{\delta}_f$	mean flap deflection angle
$\delta \mathbf{x}$	vector containing streamwise-position corrections
Γ	bound-vorticity strength
γ	elemental area of additional bound vorticity
$\mathbf{\Gamma}$	vector of the n bound-vortex strengths
ρ	density of air
σ	total induced drag of N -wing formation/ ND_{ell}
θ	local dihedral angle
θ_f	angular coordinate of flap hinge location

Subscripts

2	two-wing formation
A	wing A
av	average
B	wing B
m	mirrored image

Superscripts

0	wing root
l	left wing tip
m	centerline of wing
r	right wing tip

Chapter 1

Introduction

In the continuous effort to improve the performance and efficiency of today's aircraft, the reduction of aircraft drag has been the primary focus of many aerodynamicists. A small savings in drag can translate into significant savings in fuel usage and other costs, and this has motivated many researchers to explore innovative approaches for aircraft drag reduction. Many approaches have stemmed from the study of bird flight; the flight behavior of birds and the formation flight patterns often observed during migration have been a long-time source of inspiration to aerodynamicists. The author of a study which examines wings belonging to both bird and man states it best in saying, "Bird flight has always been one of the admitted miracles; and it remains a source of wonder even when the science of aerodynamics undertakes the explanation of the physical laws that govern it."¹ At present, there are considerable differences between the flight of birds and aircraft, the primary difference being that the aircraft wing is not used for thrust production, whereas the bird wing is capable of producing thrust as well as lift by flapping. Nevertheless, the basic flight functions of the bird and aircraft are similar, and much can still be gained from further investigation between the two. With advances in precision measurement, aircraft control, and adaptive wing technology, one can envision that future aircraft will be more capable of emulating bird flight and thus able to take advantage of the resulting low drag. Therefore,

it is worthwhile to continue exploring such drag reduction techniques as observed in nature, as they may have the potential for application to future aircraft.

In the current research, two different approaches for aircraft drag reduction were examined, where the design of each approach was motivated by bird flight studies. These two approaches are: (1) multiple spanwise trailing-edge flaps and (2) formation and ground-effect flight. In this chapter, the details and estimated benefits of each approach are presented, with a review of germane literature, including the main numerical and experimental contributions. In addition, the objectives of each study are given. An outline of the dissertation is then presented at the end of the chapter.

1.1 Multiple Spanwise Trailing-Edge Flaps

It is well known that birds are able to take advantage of their variable-geometry wings to achieve near-optimum spanwise lift distributions, thus producing minimal drag for various flight conditions. In contrast, the aircraft with rigid wings have less flexibility to adapt their wing geometry and can be optimized for only a few flight conditions. One approach that has been gaining interest over the past decade is the use of adaptive lifting surfaces. With an adaptive surface, the ideal lift distribution on a wing for any flight condition can be achieved, resulting in a reduction in drag and/or structural loads. Wing shape adaptation via spanwise camber variation can be used to not only reduce profile and induced drag, but also to alleviate structural loads at maneuvering conditions by redistributing the spanwise load distribution.

The benefits of an adaptive wing are numerous, and have been examined in numerical and experimental studies.²⁻⁶ In a study by Bolonkin and Gilyard,² the aircraft performance benefits from adaptive wing technology were estimated to be

as much as 10% at non-standard conditions and 3% at cruise conditions – benefits that can result in as much as \$300,000 per year for a transport aircraft in fuel costs alone. If the payload is increased to exploit the decrease in fuel weight, the increased revenue can be huge – as much as 30 times the cost of fuel saved.² An example of in-flight application of spanwise camber is the maneuver load control flight experiment of the AFTI/F-111 advanced-fighter aircraft³ at NASA DFRC. In this experiment, the spanwise camber flap positions were commanded as a function of flap position, true airspeed, Mach number, dynamic pressure, normal acceleration, and sweep position (of the variable-sweep wing). The measured loads indicated that the load factor can increase as much as $1.0g$ without increasing the root-bending moment. By shifting the lift load more inboard, the tip lift load was alleviated.³

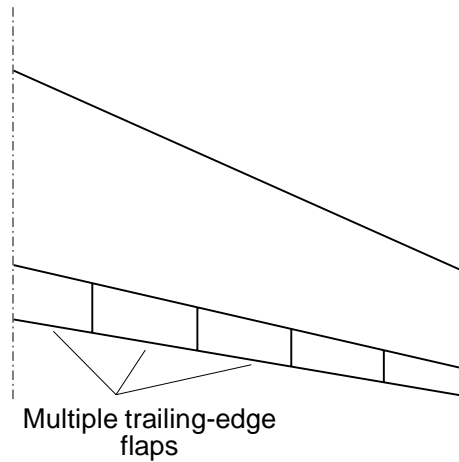


Figure 1.1: Multiple trailing-edge flaps on a swept wing.

Spanwise camber change can be accomplished by a variety of means, but one mechanism of shape adaptation attracting considerable interest is the utilization of multiple trailing-edge flaps along the wingspan, as shown in Fig. 1.1. The application of variable camber allows the sectional shape of the wing to be chosen to give minimum drag at different flight conditions. Spillman⁶ states that the

possible reductions in drag and wing weight with the use of variable camber has the potential for significant reductions in fuel usage and operating costs when compared to a fixed-geometry wing designed for the same application. Additional benefits of a wing with multiple trailing-edge flaps have been estimated and are found to be extensive,^{4,5} with more recent efforts indicating a continuing interest in adaptive wing technology in Europe.

With the estimated benefits of adaptive wing technology, and the increasing interest in multiple trailing-edge flaps, the idea of an automated adaptive wing is not too far in the future. Recent research conducted by McAvoy and Gopalarathnam^{7,8} showed the potential of automated airfoil adaptation by using a cruise flap, which was automated using flow conditions sensed at the airfoil. Like birds, which are believed to have sensory mechanisms along their span to detect span-wise aerodynamics and other atmospheric disturbances, it is believed that one day the aircraft wing will have a similar sensing capability allowing it to dynamically tailor its shape to best suit the flight condition. Therefore, in an effort to assist the larger work of developing a closed-loop control system for an adaptive wing, the objective of this particular study was to develop a method that will determine the ideal lift distributions and corresponding flap angles for the adaptive wing at different flight conditions. For the purpose of the study, low-subsonic aircraft applications with natural-laminar-flow (NLF) wings were the focus. The optimum lift distributions and flap angles at multiple operating conditions were determined for two example wings. Post-design analysis and aircraft performance simulations were used to validate the optimum flap-angle distributions as given by the developed approach and to determine the resulting improvements to aircraft performance. It is expected that the examination of this particular approach for aircraft drag reduction will provide valuable guidance toward adaptive wing technology, and will promote a near-term solution for improving aircraft performance.

1.2 Formation and Ground-Effect Flight

It is a common belief that many species of migrating birds fly together in formations for improved aerodynamic efficiency. This improved efficiency results from the upwash generated by the wings of the neighboring birds. Some of the earliest quantitative estimates of the aerodynamic benefits of formation flight were presented by Wieselsberger,⁹ who suggested that a vee-formation shape results in equal distribution of the drag benefits among all the birds in a formation. The analytical study of Lissaman and Shollenberger¹⁰ showed that a formation of 25 birds, flying with zero lateral spacing between wing tips, would have a 70% increase in range when compared to a lone bird. Similar benefits have been shown by other researchers, including Hummel^{11–13} and Hainsworth.¹⁴ Recent in-flight measurements of heart-beat rates of eight trained pelicans flying in formation and in isolation show that energy expenditure is reduced by nearly 14.5% when flying in formation,¹⁵ clearly demonstrating the benefits.

Certain species of birds, such as pelicans, can often be seen flying either solo or in formation low above the water in ground effect.¹⁶ It is well known from theoretical^{17–21} and experimental studies^{22–24} that flight in ground effect results in a reduction in the induced drag, an increase in the lift-curve slope, and an increase in the lift-to-drag ratio. It is believed that by flying close to the ground or water, birds such as the pelican are able to cover larger distances with less effort.²⁵

The concepts of formation flight and flight in ground effect have the potential for application to aircraft, and each has been studied extensively by past researchers. The advantages and issues related to aircraft formation flight have been studied analytically,^{13,26–29} in wind-tunnel experiments,^{30,31} and in flight tests.^{27,32–34} Research studies of aircraft flight in ground effect are detailed in a comprehensive literature survey by Rozhdestvensky,²⁰ which includes several

aircraft concepts designed to exploit the advantages of ground-effect flight. Many early prototypes of such aircraft first originated in Russia, where they were designed and flight tested. A more recent design concept of a flight-in-ground-effect aircraft is the Boeing Pelican.³⁵ Past theoretical aerodynamic studies include the development of approaches for determining the optimum lift distributions and associated minimum induced drag values for formation flight,^{28,29,36} ground-effect flight,^{18,19,36} and combined formation and ground-effect flight.³⁷⁻³⁹ These methods have typically used Lagrange-multiplier-based constrained-minimization approaches^{26,40,41} or optimum-downwash^{29,39} approaches implemented using vortex-lattice formulations, or were developed using exact solutions.^{19,38}

While many previous investigations have studied the benefits of formation flight^{9-13,27,30-34} and ground effect,¹⁸⁻²⁴ it must be noted that the benefits of combined formation and ground-effect flight have not received as much attention, even though migrating birds have been observed flying in formation close to the water surface.¹⁶ One exception is the work of McMasters and McLean,³⁷ in which an analytical study was used to propose that two human-powered aircraft flying in formation close to the water could successfully complete the flight across the English Channel for the £100,000 Kremer prize,⁴² which was subsequently won by the flight of the Gossamer Albatross^{42,43} in 1979. Any additional attention to the benefits of combined formation and ground-effect flight was not received until just recently. In 2004, the results of the current research were published as an AIAA conference paper⁴⁴ and are to appear in *Journal of Aircraft*.⁴⁵ Also in 2004, Marino³⁹ presented an aerodynamic model based on lifting line theory, which was used to determine optimum formation configurations in and out of ground effect for minimum induced drag, taking into account both the geometrical and aerodynamic parameters of the aircraft. And most recent is the work of Lissaman,³⁸ in which an exact analytical formulation using complex variables was developed to

determine the theoretical savings in drag obtainable for wing formations in and out of ground effect.

While the estimated benefits of formation and ground-effect flight, as deduced in theory and from experimental measurements, are substantial, significant issues in maintaining proper aircraft position have thus far prevented the widespread use these techniques for aircraft drag reduction. However, with advances in precision measurement, control of the relative position of aircraft, and as discussed earlier, the development of adaptive-wing technology, formation flight and ground-effect flight is attracting a renewed interest^{35,36,46,47} as feasible drag-reduction approaches for future aircraft. The realization of their everyday use is still far from the present, but the potential drag savings these flight techniques provide will revolutionize aircraft aerodynamic efficiency.

Therefore, as the second part of the presented research, it was of interest to further examine the benefits of formation flight and ground-effect flight, in particular the benefits of combined formation and ground-effect flight, as another approach for aircraft drag reduction. For this purpose, optimally-loaded planar and non-planar wings, as well as elliptically-loaded planar wings, were examined in order to determine the lower limit in induced drag attainable for any given formation and ground-effect geometry. For this particular study, the optimum-downwash approach of Frazier and Gopalarathnam²⁹ was used for the study of optimally-loaded wings, and exact solutions were developed for the study of elliptically-loaded wings. Specific attention was paid to the effect of lateral separation and to the favorable/adverse interference effects between different pairs of wings in formation and ground-effect configurations. It is believed that the results presented for this drag-reduction approach will help to further advance the idea that formation flight and flight in ground-effect can be a viable alternative for improving the performance and efficiency of tomorrow's aircraft.

1.3 Outline of Dissertation

Chapter 2 presents the study of multiple spanwise trailing-edge flaps as an approach for reducing aircraft drag. The chapter begins with background information relevant to the development of the approach for determining optimum trailing-edge flap angles for different flight conditions. The details of the approach are then presented, including the procedure for obtaining flap schedules for minimum drag with an optional root-bending moment constraint. The remaining portion of the chapter presents two example wings: (1) a planar wing, and (2) a nonplanar wing. The determined optimum flap schedules are presented for each wing for various flight conditions, subject to a root-bending moment constraint. The results of a post-design analysis and aircraft performance simulations are also presented to validate the optimum flap-angle distributions determined using the current method.

Chapter 3 presents the study of combined formation and ground-effect flight as a second approach for aircraft drag reduction. The details of the numerical approach are first presented, which address the procedure taken to determine the optimum lift distribution for minimum induced drag, the simulation of ground-effect, the prescription of the elliptical lift distribution and the development of the exact approach for elliptically loaded wings, and the determination of the optimum vee-formation shape. Presented next is the validation of the optimum-loading method. Lastly, the results are presented, which focus on three main topics: (1) the effect of lateral separation on the drag benefits for formations flying out of ground effect, (2) the benefits of combined formation and ground-effect flight, and (3) the optimal vee-shapes of formations.

Chapter 4 presents some concluding remarks regarding the two approaches for drag reduction, and Chapter 5 presents some suggested future work.

Chapter 2

Ideal Lift Distributions and Flap Angles for Adaptive Wings

As the first portion of this dissertation, this chapter presents in detail the study of multiple spanwise trailing-edge (TE) flaps as an approach for adapting a wing to suit flight conditions. In the effort to assist in the larger work of developing a closed-loop control system for an adaptive wing, the main objective of this study was to develop a method that determines ideal lift distributions and corresponding TE flap deflection angles at different flight conditions. Low-subsonic aircraft applications with natural-laminar-flow (NLF) wings were the focus of the study, with results presented for two example wings: (1) a planar wing, and (2) a nonplanar wing. In the following sections, background information relevant to the development of the approach is presented, followed by a detailed methodology of the approach. The results are then presented, which include the determined optimum lift distributions and corresponding flap angles for each example wing at multiple operating conditions subject to a root-bending moment (RBM) constraint. The results from a post-design analysis and aircraft performance simulations used to validate the determined optimum flap-angle distributions are also presented to establish the improvements made to aircraft performance. A summary of the study and its findings are given at the end of the chapter.

2.1 Background

This section includes background information relevant to the development of the approach for determining optimum TE flap angles for different flight conditions. The methodology is built on three well-known elements in applied aerodynamics, which are presented here in subsections. The first subsection describes the approach taken to determine the optimum lift distribution for minimum induced drag with or without a wing RBM constraint. The second subsection describes the use of thin airfoil theory relations to determine the C_l -shift in the drag bucket of an NLF airfoil due to TE flap deflection. The theory of additional and basic lift distributions is then presented in the third subsection.

2.1.1 Minimum Induced Drag with and without Root-Bending Moment Constraint

For 1- g flight, at high C_L , the dominant consideration in wing drag is often the induced drag. For planar wings, the optimum lift distribution for minimum induced drag is the well-known elliptical loading. Multiple TE flaps can be used to adjust the spanwise lift distribution and bring it close to the optimum distribution. On the other hand, for high- g flight, the most important consideration is the structural loading on the wing, especially at the wing root, as it often determines the design of the internal wing structure and the resulting wing weight. Proper deflection of TE flaps can redistribute the spanwise loading on the wing in high- g flight to relieve the loading at the wing tip and thus alleviate the RBM. Hence, for the purpose of determining optimum TE flap angles for different flight conditions, a numerical method was first developed to determine the optimum lift distribution on a wing that will result in minimum induced drag with the option of a RBM constraint.

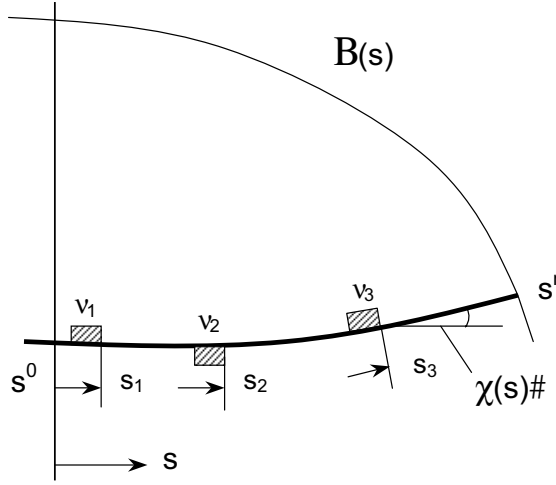


Figure 2.1: Spanwise load curve on a nonplanar wing with three elements of variation.

The methodology of the numerical approach was based on the work of R. T. Jones,⁴⁸ and was extended to handle nonplanar wings, each with an arbitrary spanwise variation of dihedral. In this method, the optimum downwash behind the wing is first determined using the calculus-of-variation approach of Jones.⁴⁸ The wake is assumed to be rigid and invariant with the streamwise direction, as it is assumed to trail behind the wing in the direction of the freestream. Figure 2.1 is an illustration of a lift distribution on a symmetric nonplanar wing with spanwise curvature. The lift distribution, referred to as the original lift distribution, is designed to achieve minimum induced drag. The position along the wake trace of the wing is denoted using the arc length s and the local dihedral angle at any spanwise location is $\theta(s)$. The bound vortex distribution, Γ , associated with the original lift distribution can be used to compute the lift on the wing by spanwise integration as shown in Eq. 2.1.

$$L = 2\rho V_\infty \int_{s^0}^{s^r} \Gamma(s) \cos[\theta(s)] ds \quad (2.1)$$

The wing RBM due to the lift distribution can also be computed from the Γ distribution, and is shown in Eq. 2.2. The function $q(s)$, shown in Eq. 2.3, is the contribution to the RBM due to a unit load acting normal to the wing at s .

$$RBM = \rho V_{\infty} \int_{s^0}^{s^r} \Gamma(s) q(s) ds \quad (2.2)$$

$$q(s) = \cos [\theta(s)] [y(s)] - \sin [\theta(s)] [z(s)] \quad (2.3)$$

To compute the induced drag of the wing due to this lift distribution, the Trefftz-plane normalwash distribution $w(s)$ is used in addition to the Γ distribution, as shown in Eq. 2.4.

$$D = \rho \int_{s^0}^{s^r} w(s) \Gamma(s) ds \quad (2.4)$$

The goal of the current method is to determine the downwash distribution behind the wing that will result in a minimum in the induced drag while satisfying constraints on the desired lift and desired RBM on the wing. As presented by Jones,⁴⁸ a change in the induced drag due to a small variation in Γ , referred to as additional distribution, is composed of three parts:

1. The drag arising from the additional Γ distribution acting on the additional Trefftz-plane downwash distribution
2. The drag arising from the original Γ distribution acting on the additional Trefftz-plane downwash distribution
3. The drag arising from the additional Γ distribution acting on the original Trefftz-plane downwash distribution

The first part is a second-order term and can be neglected when compared to the other two parts. From Munk's mutual drag theorem,⁴⁹ the second and third parts

of the additional induced drag are equal. Therefore, if the first-order change in the wing induced drag is to be zero then it is sufficient to set the drag arising from the additional Γ distribution acting on the original Trefftz-plane downwash distribution (third part) to zero.

In order to satisfy the constraints on the specified lift and root-bending moment, the additional Γ distribution should be selected such that it generates no additional lift or root-bending moment for the wing. Using the arguments of Jones,⁴⁸ an additional distribution meeting these requirements must be subdivided into at least three elements. Thus, as seen in Fig. 2.1, the additional Γ distribution can be represented by three small elements having areas γ_1 , γ_2 , and γ_3 , and arbitrarily located at s_1 , s_2 , and s_3 along the wing.

If the original Γ distribution represents the optimum loading, then the additional Γ distribution must satisfy the following conditions: (1) there should be no change in lift on the wing (Eq. 2.5), (2) there should be no change in the RBM (Eq. 2.6), and (3) there should be no change in the induced drag (Eq. 2.7). In Eq. 2.7, w_1 , w_2 , and w_3 are the Trefftz-plane normalwash values associated with the original Γ distribution at the corresponding locations s_1 , s_2 , and s_3 .

$$\gamma_1 \cos [\theta(s_1)] + \gamma_2 \cos [\theta(s_2)] + \gamma_3 \cos [\theta(s_3)] = 0 \quad (2.5)$$

$$\gamma_1 q(s_1) + \gamma_2 q(s_2) + \gamma_3 q(s_3) = 0 \quad (2.6)$$

$$\gamma_1 w_1 + \gamma_2 w_2 + \gamma_3 w_3 = 0 \quad (2.7)$$

It can be seen that in order to satisfy Eqs. 2.5–2.7, the original Trefftz-plane normalwash along the wake traces of the wing must be of the form $w(s) =$

$A \cos[\theta(s)] + Bq(s)$, where A and B are constants that are determined using the specified values of the lift and root-bending moment for the wing. When no RBM constraint is specified, $B = 0$ and the optimum downwash is seen to be proportional to the cosine of the local dihedral angle, as was first shown by Munk.⁴⁹ This results in a constant downwash for a planar wing with no RBM constraint.

The Γ distribution on the wing and the associated Trefftz-plane downwash distribution w behind it are closely related and can be determined using a discrete vortex method similar to that described by Blackwell.⁵⁰ The bound vorticity distribution and the trailing vorticity shed behind it are approximated using n horseshoe vortices, each having a constant value for the bound vortex strength Γ . With such a formulation, the n -dimensional Γ vector and the n -dimensional \mathbf{w} vector can be related using an $n \times n$ influence coefficient matrix \mathbf{I} as shown in Eq. 2.8. For a known \mathbf{w} , the Γ distribution can be computed by solving Eq. 2.8 and the lift, root-bending moment, and induced drag can then be determined using Eqs. 2.1–2.4.

$$\mathbf{I} \cdot \Gamma = \mathbf{w} \quad (2.8)$$

For the current problem, $w(s)$ for the wing is known in terms of the two unknown constants A and B . These unknowns are computed using a single step of Newton’s method as shown in Eq. 2.9. The solution is made simple because of the fact that zero values for A and B correspond to zero values for L and RBM. The Jacobian of partial derivatives is computed using finite differencing. For example, $\partial L / \partial A$ is computed by making a small change to A and computing the change to L . The right hand side is a vector of the desired values of lift L and root-bending moment RBM. Thus the unknown constants A and B can be determined using Eq. 2.9, and can then be used to determine the Trefftz-plane

downwash. The Γ distribution is then computed, from which other quantities can be determined using Eqs. 2.1–2.4.

$$\begin{pmatrix} \frac{\partial L}{\partial A} & \frac{\partial L}{\partial B} \\ \frac{\partial RBM}{\partial A} & \frac{\partial RBM}{\partial B} \end{pmatrix} \begin{pmatrix} A \\ B \end{pmatrix} = \begin{pmatrix} L \\ RBM \end{pmatrix} \quad (2.9)$$

The relationship between a specified wing RBM constraint and the resulting Trefftz-plane downwash is illustrated for a planar wing in Fig. 2.2(a). The wing of aspect ratio 20 is required to operate at a wing C_L of 1.0, while satisfying a user-specified RBM constraint. The computed Trefftz-plane downwash distributions along the right half-span of the wing are presented for the wing without any RBM constraint and for the wing with different RBM constraints. The case where no RBM constraint is applied corresponds to flight at $1.0g$, and is considered the baseline case with a calculated root-bending moment coefficient C_{RBM} of 0.1061 ($= C_{baseline}$). For the cases where a RBM constraint is applied, the C_{RBM} is expressed in terms of $C_{baseline}$ as a point of reference. It can be seen that the optimum downwash is constant along the wingspan for the baseline case of flight at $1.0g$. With the application of decreasing RBM constraint values, the slope of the computed downwash distribution increases to the point that upwash is experienced at the Trefftz-plane behind the wing tip, as seen for the cases of $0.83C_{baseline}$ and $0.77C_{baseline}$.

Figure 2.2(b) shows the corresponding nondimensionalized lift distributions computed using the downwash distributions presented in Fig. 2.2(a). For the baseline case, where no RBM constraint is applied, the well-known elliptical lift distribution results. However, when decreasing RBM constraint values are applied, the resulting lift distribution becomes less elliptical, and more “bell” shaped as the

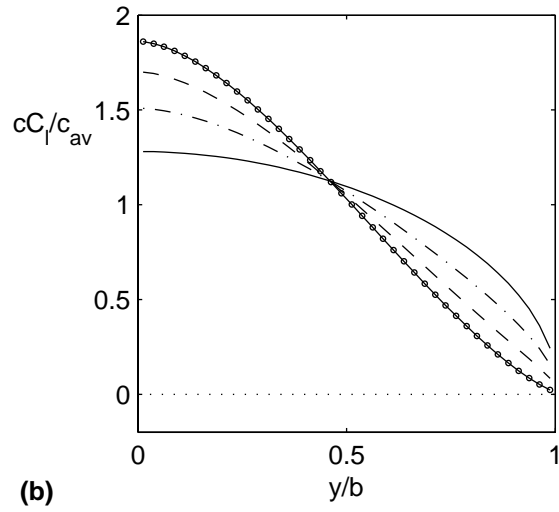
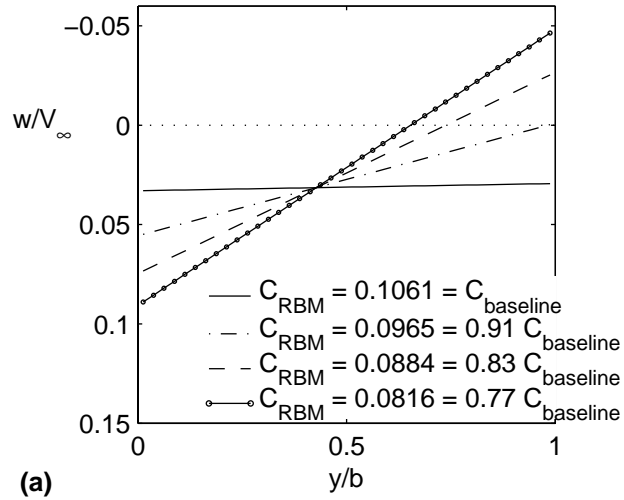


Figure 2.2: Single symmetric wing with different RBM constraints: (a) Trefftz-plane downwash distributions, and (b) nondimensionalized spanload distributions.

wing lift is shifted more inboard. This redistribution of lift decreases the amount of lift experienced at the wing tip, alleviating the RBM to meet the specified RBM constraint, and thus demonstrating the ability of the method to successfully determine an optimum lift distribution for minimum induced drag with a RBM constraint.

2.1.2 Minimum Profile Drag

For flight at low subsonic Mach numbers, wing profile drag is dominated by skin-friction drag when there is no separated flow and associated pressure drag. To minimize profile drag, airfoils are often designed to have significant regions of favorable pressure gradients on both upper and lower surfaces to support laminar flow. Such natural laminar flow (NLF) airfoils typically have a distinct low-drag range (LDR) or drag bucket, which is the range of lift coefficients over which low drag is achieved. When operating within the LDR, the airfoil leading-edge stagnation point is located within a small desirable region that results in favorable pressure gradients on both the upper and lower surfaces. The wing angle of attack at which the stagnation point is exactly at the optimum location on the leading edge of the airfoil is known as the α_{ideal} . When operating outside the LDR, the stagnation point is located outside the desirable region and there is a suction peak on either the upper or the lower surface at the leading edge. This suction peak causes a transition from laminar to turbulent flow and the skin-friction drag increases as a result. Figure 2.3 illustrates how the stagnation-point location on an airfoil varies with α by considering three different angles of attack: 1) $\alpha < \alpha_{ideal}$, 2) $\alpha = \alpha_{ideal}$, and 3) $\alpha > \alpha_{ideal}$.

The approximate C_l corresponding to the middle of the LDR for an NLF airfoil can be estimated using thin airfoil theory. This is accomplished by using the C_l that corresponds to the condition at which the stagnation point is exactly at the

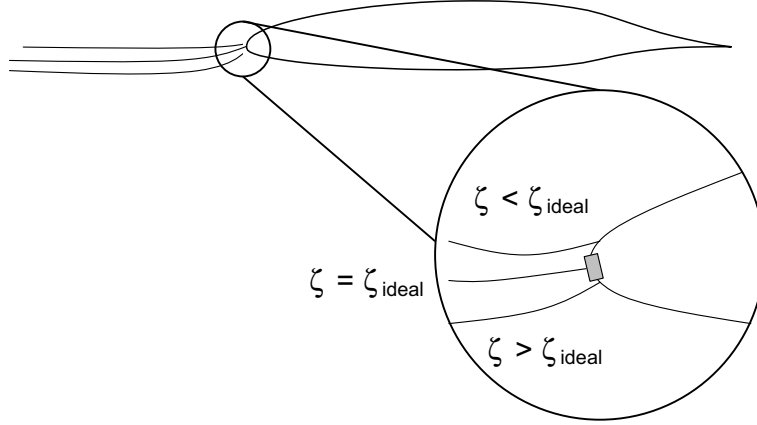


Figure 2.3: Location of leading-edge stagnation point on an airfoil.

leading edge of the thin airfoil. At this C_l , referred to as $C_{l_{ideal}}$, there is no leading-edge singularity in the chordwise vorticity distribution. For a given camberline, the $C_{l_{ideal}}$ and the α_{ideal} correspond to the condition at which $A_0 = 0$, where A_0 is the first coefficient in the Fourier series²¹ that is typically used to model the vorticity distribution in thin airfoil theory. It can be shown that the $C_{l_{ideal}}$ occurs at $\alpha = 0$ deg for an unflapped airfoil. As a result, with increase in camber, the $C_{l_{ideal}}$ increases.

To extend the range of lift-coefficients over which low drag is achieved, a trailing-edge “cruise” flap is often used. First introduced by Pfenninger,^{51,52} it has since been used on several airfoil designs,^{53–59} especially on airfoils for high-performance sailplanes.⁵⁷ Deflecting a trailing-edge flap results in a change to the $C_{l_{ideal}}$ of the airfoil and as a consequence, the C_l for the middle of the LDR of an airfoil can be changed by changing the flap angle. It can be shown from thin airfoil theory that the change to the $C_{l_{ideal}}$ due to a flap deflection δ_f is:

$$\Delta C_{l_{ideal}} = (\pi A_1) \delta_f = (2 \sin \theta_f) \delta_f \quad (2.10)$$

where δ_f is the flap angle in radians and A_1 is one of the coefficients in the Fourier series for the chordwise vorticity distribution in thin airfoil theory.²¹ The angular coordinate for the hinge location θ_f in radians is related to x_f/c as shown in Eq. 2.11.

$$\theta_f = \cos^{-1} \left(1 - 2 \frac{x_f}{c} \right) \quad (2.11)$$

Thus, Eq. 2.10 can be used to determine the C_l -shift of the LDR of an airfoil due to a flap deflection δ_f . If an assumption is made that the C_l -width of the LDR is independent of the flap angle, then the C_l -shift given by Eq. 2.10 is also the change in the C_l values for the upper and lower corners of the LDR due to a given flap angle.

2.1.3 Basic and Additional Lift Distributions

The focus of the current study was to develop an approach for determining the TE flap angles to achieve a desired spanwise lift distribution. A key part of the approach is the concept of basic and additional lift distributions, the fundamentals of which are described in several references.^{60–62} The use of this concept enables the determination of flap angles using simple analytical expressions. In this subsection, this concept is briefly reviewed and extended for the current application to nonplanar wings with multiple flaps.

Within the assumption of linear aerodynamics (linear C_l - α slope and linear C_l - Γ relationship), the distribution of lift over a wing can be divided into two parts: (i) basic lift, L'_b and (ii) additional lift, L'_a . For a given wing with a specified chord distribution, the C_l distribution can also be considered as a sum of two parts: (i) the basic lift-coefficient distribution, C_{lb} , and (ii) the additional lift-coefficient distribution, C_{la} :

$$C_l = C_{lb} + C_{la} \quad (2.12)$$

C_{lb} is the C_l distribution at $C_L = 0$, and is the result of spanwise variations in geometric twist, aerodynamic twist due to camber, and flap deflections. Furthermore, the C_{lb} distributions due to twist, camber, or flap deflection, scale linearly with that particular parameter, and individual C_{lb} distributions can be added to equal the total C_{lb} distribution. For example, the C_{lb} due to combined wing twist, camber change, and flap-angle variation is simply the sum of the individual C_{lb} distributions:

$$C_{lb} = C_{lb,twist} + C_{lb,camber} + C_{lb,\delta_f} \quad (2.13)$$

It can also be shown that for an arbitrary nonplanar wing, spanwise twist or camber variations that are proportional to the cosine of the local dihedral angle θ do not contribute to the C_{lb} , because they are equivalent to changes in the wing α .

C_{la} is the additional C_l distribution due to α with zero geometric and aerodynamic twist. It is, therefore, independent of geometric or aerodynamic twist and scales with wing C_L . Thus, the C_{la} for $C_L = 1$ can be precomputed for a wing and used to compute the C_{la} for any C_L , as shown in Eq. 2.14,

$$C_{la} = C_L C_{la,1} \quad (2.14)$$

where $C_{la,1}$ is the C_l distribution for the given wing with no geometric or aerodynamic twist at a C_L of 1.0.

For illustration of the concept, an example wing with a vertical winglet of height $0.125b$ is considered. This wing was analyzed using the WINGS code, which

is a discrete-vortex Weissinger's method code. Four TE flaps are located spanwise along the planar portion of the wing, with one flap on the winglet, each flap having the same span and flap-to-chord ratio of 0.2. In this particular example, the wing is assumed to have no geometric twist and zero section camber. In Fig. 2.4(a), $C_{la,1}$ for the wing, as computed using WINGS, is shown. Also shown are the C_{lb} distributions from WINGS for 1-deg deflections of (i) flap 4, which is the flap at the tip of the planar portion and (ii) flap 5 located on the winglet. These C_{lb} distributions have been plotted using a magnification of five for clarity.

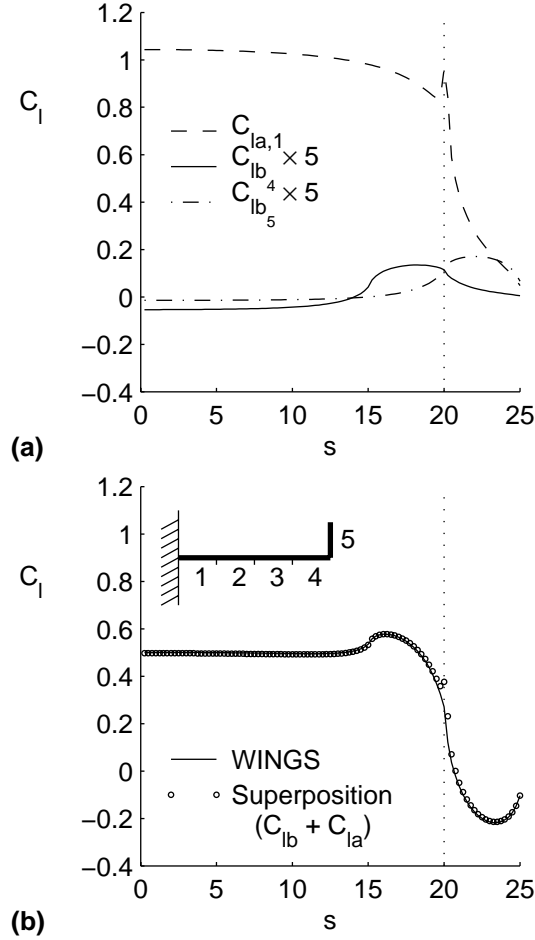


Figure 2.4: Lift distribution for wing with winglet, (a) additional and basic lift and (b) C_l due to superposition in comparison to C_l from WINGS. Inset in (b) shows rear view of nonplanar wing with five flaps.

The C_l distribution for this wing at $C_L = 0.5$ with flap 4 deflected to $\delta_f = 5$

deg, and flap 5 deflected to $\delta_f = -10$ deg, was then computed using the WINGS code. This distribution is compared in Fig. 2.4(b) to the distribution achieved by superposition of (i) $C_{l_{a,1}}$ scaled by 0.5, (ii) C_{l_b} for flap 4 scaled by 5, and (iii) C_{l_b} for flap 5 scaled by -10 . The excellent comparison illustrates the concept of superposition of C_l distributions.

The advantage of using the superposition concept is that the net C_l distribution for a particular wing C_L can be posed in terms of the unknown flap angles and can be equated to a desired C_l distribution. By constructing these equations to represent the airfoil sections located at the middle spanwise location of each flap, the equations can be solved to determine the flap angles corresponding to the desired C_l distribution.

2.2 Methodology

The methodology presented in this section includes the approach taken to determine the flap angles for either minimizing drag or for minimizing drag subject to a constraint on the wing RBM. In this approach, the airfoil section at the middle of each flap is considered and will be referred to as a “control section” in the remainder of this chapter. At the specified wing C_L , the C_l at each of these control sections is expressed in terms of the C_{l_a} distribution and the C_{l_b} distribution, which contains the unknown flap angles. The C_l values at the control sections are then set equal to the desired C_l values for these locations. Thus, for a wing with m flaps, this approach results in m simultaneous linear equations that need to be solved to obtain the m unknown flap angles.

Equation 2.15 shows the general form of the equations:

$$C_L\{C_{l_{a,1}}\} + \{C_{l_{b,twist}}\} + \{C_{l_{b,camber}}\} + [C_{l_{b,f}}]\{\delta_f\} = \{C_{l_{desired}}\} \quad (2.15)$$

Each of the terms in the curly brackets are vectors with m values. The $C_{l_{b,f}}$ is a square matrix whose (i, j) element is the C_{l_b} at the i^{th} control section for a unit deflection of the j^{th} flap. Thus for a given planform, twist and camber distributions, an analysis method such as the WINGS code is used to determine $\{C_{l_{a,1}}\}$, $\{C_{l_{b,twist}}\}$, and $\{C_{l_{b,camber}}\}$. The code is then used m times to compute $\{C_{l_b}\}$ for the unit deflection of each flap to fill the $[C_{l_{b,f}}]$ matrix. All of these values are independent of C_L and δ_f and do not need to be recomputed. The solution for the desired flap angles for any flight condition can then be determined by solving the m simultaneous equations.

2.2.1 Flap Angles for Minimum Drag

For most wings, it is possible to achieve minimum-induced-drag loading (elliptical loading for a planar wing) and also ensure that each control section is operating in the low-drag range (LDR). For such cases, the $C_{l_{desired}}$ can be written in terms of the optimum lift distribution, $C_{l_{opt}}$, for $C_L = 1$, obtained using the method described in Sec. 2.1.1.

$$C_L\{C_{l_{a,1}}\} + \{C_{l_{b,twist}}\} + \{C_{l_{b,camber}}\} + [C_{l_{b,f}}]\{\delta_f\} = C_{l_{opt}} = C_L\{C_{l_{opt,1}}\} \quad (2.16)$$

By solving the system of equations for a design C_L , the resulting flap deflection angles $\{\delta_f\}$ can be obtained. $\{\delta_f\}$ can be written as a sum of a “mean” flap angle $\bar{\delta}_f$ and a spanwise flap-angle distribution $\{\hat{\delta}_f\}$ about that mean as seen in Eq. 2.17.

$$\{\delta_f\} = \bar{\delta}_f + \{\hat{\delta}_f\} \quad (2.17)$$

The mean flap angle is set so that most of the wing is operating within the low-drag range, and the spanwise flap-angle distribution $\{\hat{\delta}_f\}$ will be used to minimize the induced drag. With that objective, the mean flap angle can be determined using:

$$\bar{\delta}_f = \frac{C_L - C_{Lideal}}{2 \sin \theta_f} \quad (2.18)$$

where C_{Lideal} is the C_L corresponding to a point within the drag bucket of the unflapped airfoil being used, and $(2 \sin \theta_f)$ is the C_l -shift of the drag bucket due to flap deflection. C_{Lideal} is determined using Eq. 2.19, which is also valid for nonplanar wings.

$$C_{Lideal} = \frac{2}{S} \int_{s^0}^{s^r} c C_{lideal} \cos \theta ds \quad (2.19)$$

In addition to determining the optimum flap angles, this approach also outputs the corresponding desired C_l values at each control section using Eq. 2.16.

2.2.2 Flap Angles for Minimum Drag with a RBM

Constraint

Similar to the procedure for minimizing drag, the flap angles for minimum drag with a RBM constraint are computed by selecting the desired C_l distribution to correspond to a lift distribution that results in minimum induced drag while satisfying the specified RBM constraint. This desired lift distribution, C_{lRBM} , is obtained using the same procedure described in Sec. 2.1.1 for a desired RBM at $C_L = 1.0$. The following system of equations is then solved for the design C_L to

determine $\{\delta_f\}$, which can be written as a sum of $\bar{\delta}_f$ and $\{\hat{\delta}_f\}$, as demonstrated in the previous subsection.

$$C_L\{C_{la,1}\} + \{C_{lb,twist}\} + \{C_{lb,camber}\} + [C_{lb,f}]\{\delta_f\} = C_{lRBM} = C_L\{C_{lRBM,1}\} \quad (2.20)$$

2.3 Results

Two examples are presented in this section to demonstrate the approach for determining the optimum flap angles for various flight conditions. Post-design analysis using the WINGS code and aircraft performance simulations are used to verify the results from the approach.

2.3.1 Example 1: Planar Wing

For this example, a planar wing of aspect ratio 12 for a hypothetical general aviation aircraft is used. Table 2.1 lists the overall specifications of the hypothetical aircraft. Figure 2.5 shows the wing-tail geometry used for the hypothetical aircraft. For the adaptive wing, five TE flaps have been used along the half span, each with equal span and a flap-to-chord ratio of 0.2. The tail has been used for trimming the aircraft about the center-of-gravity, which is located to result in a stick-fixed static margin of 10% of the wing mean aerodynamic chord. A single airfoil, custom designed for this wing, using the method of Ref. 63, has been used along the span and the wing twist is assumed to be zero.

Figure 2.6(a) shows the airfoil geometry and velocity distribution, and Fig. 2.6(b) shows the drag polar for the airfoil at $Re\sqrt{C_l} = 3$ million, as computed using the XFOIL code.⁶⁴ This value of $Re\sqrt{C_l}$ corresponds to rectilinear flight at standard

Table 2.1: Assumed geometry, drag, and power characteristics for the hypothetical general aviation airplane for Example 1.

Parameter	Value
Gross Weight (W)	14200 N (3200 lbf)
Wing reference area (S)	12.0 m^2 (130 sq.ft.)
Wing aspect ratio (AR)	12
Equivalent parasite drag area of airplane minus wing ($C_{Df}S_f$)	0.13 m^2 (1.4 sq.ft.)
Rated engine power (P_{av})	200 kW (268 hp)
Specific fuel consumption (sfc)	8.31×10^{-7} N/s/W (0.5 lbf/h/hp)
Fuel volume	300 liters (80 U.S. gallons)

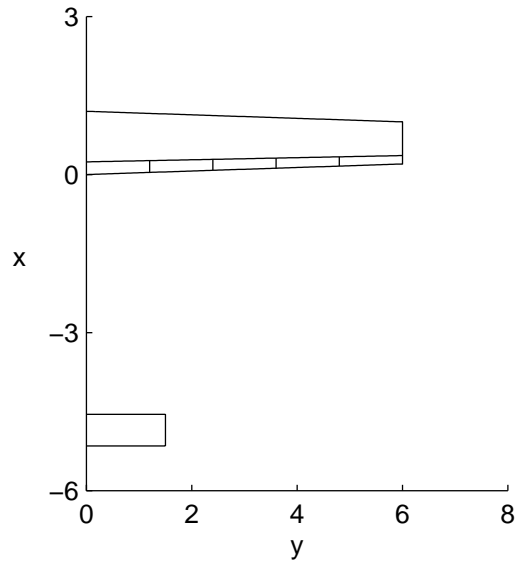


Figure 2.5: Wing and tail geometry for Example 1.

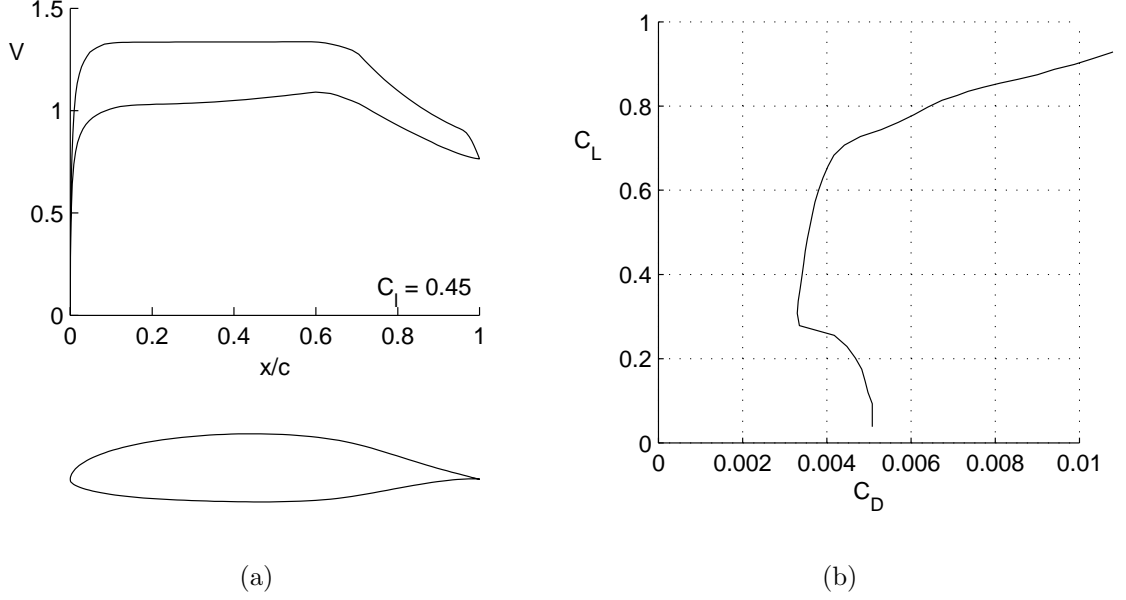


Figure 2.6: Airfoil for Example 1: (a) geometry and velocity distribution, and (b) drag polar at $Re\sqrt{C_l} = 3 \times 10^6$.

sea-level conditions. It is seen that the airfoil LDR extends from $C_l = 0.3$ to $C_l = 0.7$ for the unflapped airfoil. Using the information in this polar and the airfoil-aircraft integration approach described in Ref. 65, the ideal C_L for level-flight maximum speed for the aircraft was determined to be approximately 0.15 and the ideal C_L for the maximum range was determined to be 0.73. Based on these estimates, it was decided that the wing would need to be adapted for low drag over a range of lift coefficients from 0.1 to 0.9. For determining the optimum flap scheduling, it was decided that the $C_{l_{ideal}}$ used as input in the current approach would vary linearly from 0.3 to 0.7 for values of the wing C_L ranging from 0.1 to 0.9.

In this example, because the mean flap angle $\bar{\delta}_f$ for each C_L is selected to result in the wing operating within the LDR, the flap angles for minimum induced drag also result in the extensive laminar flow on all the sections. As a result, both profile and induced drag are minimized over the entire C_L range.

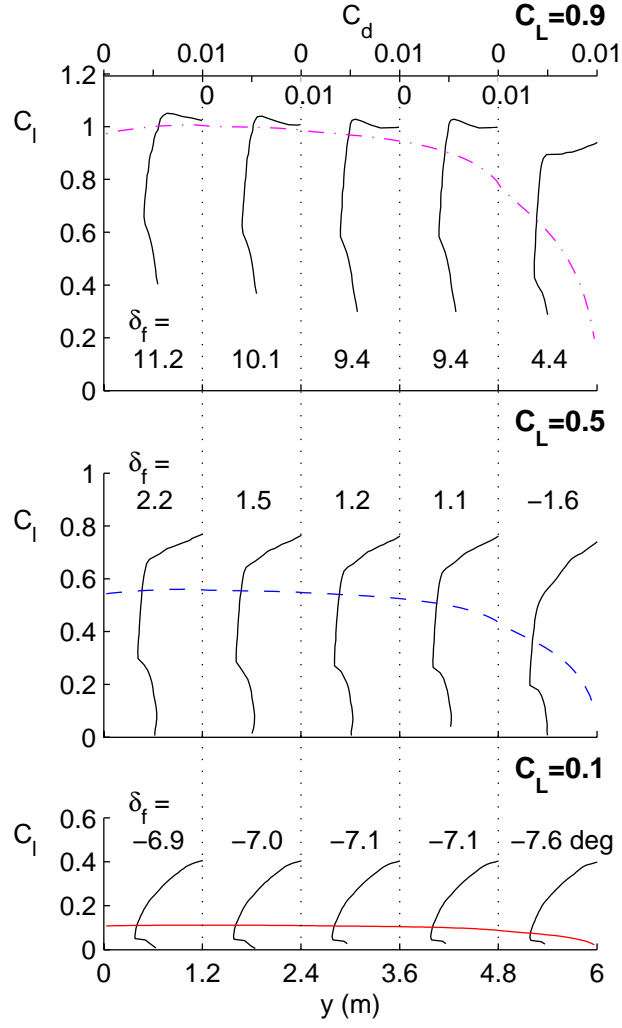


Figure 2.7: Spanwise C_l distributions and drag polars for flaps optimized for $C_L = 0.1, 0.5$, and 0.9 .

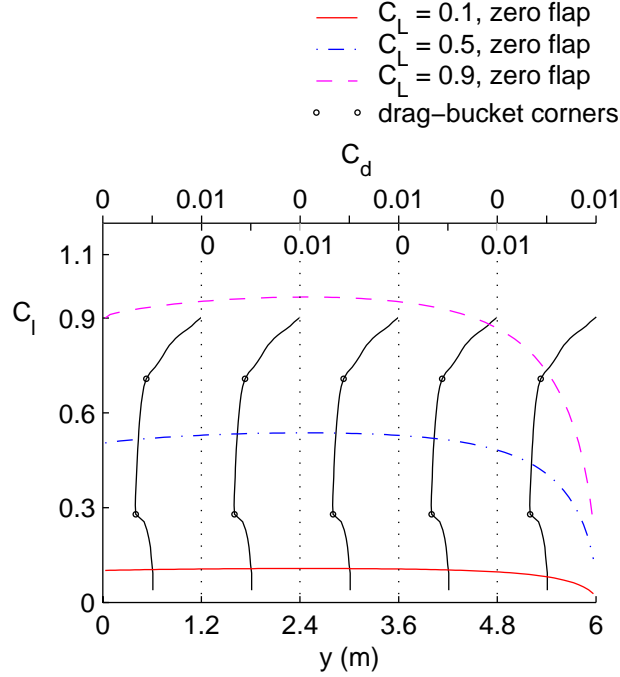


Figure 2.8: Spanwise C_l distributions and drag polars for the non-adapted wing (all flaps set to zero deg).

Figure 2.7 shows the spanwise C_l distributions from the WINGS code for three values of the design C_L : 0.1, 0.5, and 0.9. In each case, the flaps were set to the optimum angles, as determined by the current approach. Superposed on each of the spanwise- C_l plots are the drag polars (section C_d - C_l plots) for each control section from XFOIL analysis, with the five C_d scales on top of the plot. Each control section is also labeled with the corresponding flap angle. The results demonstrate that the optimum flap-angle distribution ensures that each section C_l corresponds to a point within the appropriate drag bucket. Also to be noted is that the flap angle for any given section varies smoothly with the flight condition. To put this in perspective, Fig. 2.8 shows the C_l distributions for the non-adapted wing with all flaps set to zero deg, for the three wing C_L values and the corresponding section drag polars for $\delta_f = 0$. It is seen for $C_L = 0.1$ and 0.9 , the section C_l values for most of the wing do not lie within the LDR, indicating

that these portions of the wing do not have extensive laminar flow.

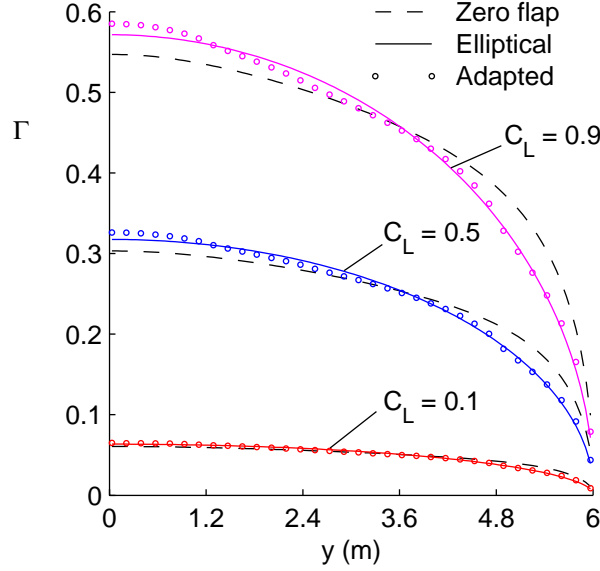


Figure 2.9: Spanwise Γ distributions for $C_L = 0.1$, 0.5 , and 0.9 , for the adapted and non-adapted wings compared with the elliptical loading.

Figure 2.9 shows the spanwise Γ distributions for these three values of C_L for the adapted wing with optimum flap angles as well as for the non-adapted wing with all flaps set to zero deg. The minimum-induced-drag elliptical Γ distribution, shown for reference, reinforces the fact that the Γ distribution for the adapted case for each C_L closely matches the desired elliptical loading.

In order to determine that the predicted flap-angle distributions are indeed the best for each C_L , post-design analysis and aircraft performance prediction were used. First, the wing with the flap schedules was analyzed using the WINGS code at the three values of C_L . In these analyses, the contributions due to both the trimmed-aircraft induced and profile drag were computed by including the C_{dp} estimates from XFOIL⁶⁴ for each section at the corresponding section C_l and δ_f . Figure 2.10 presents the total wing C_D as a function of wing C_L for four cases: (i) all flaps set to zero, (ii) flaps set for $C_L = 0.1$, (iii) flaps set for $C_L = 0.5$, and (iv) flaps set for $C_L = 0.9$. It is clearly seen that the optimum flap schedule for a given

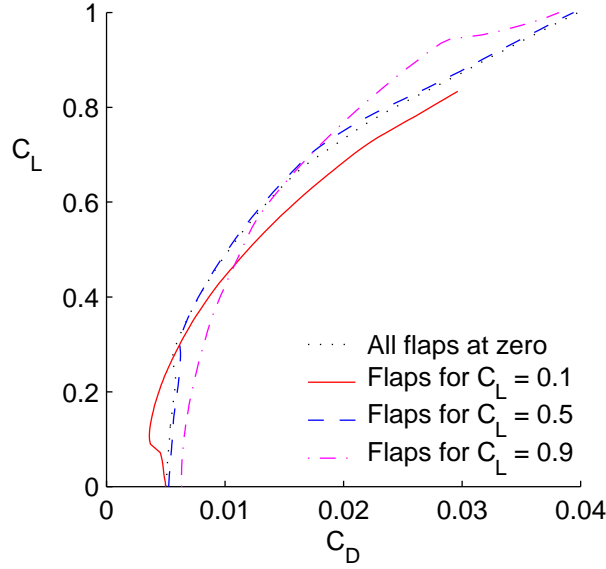


Figure 2.10: Drag polars for zero flaps, and flaps optimized for $C_L = 0.1$, 0.5 , and 0.9 .

C_L , as determined by the current approach, results in the least drag at that C_L . This result demonstrates the effectiveness of the current approach in determining the optimum flap angles for a given C_L .

In order to examine the performance benefits due to the different flap-angle variations, the drag predictions from WINGS was used in PERF, an aircraft-performance code. Figures 2.11(a)–(c) show comparisons of the aircraft rate of climb, range, and endurance as a function of airspeed at standard sea-level conditions. The results show that (1) for the case with the flaps optimized for $C_L = 0.1$, the V_{max} is significantly greater than all of the other cases by around 10 mph and (2) the case with the flaps optimized for $C_L = 0.9$ results in the maximum range, and the maximum endurance, with the maximum endurance a 12% improvement when compared to the case with all flaps set to zero. This performance comparison clearly illustrates the benefits of the flap-optimization approach developed in the current study.

In the next part of the study with this example wing, the use of multiple TE

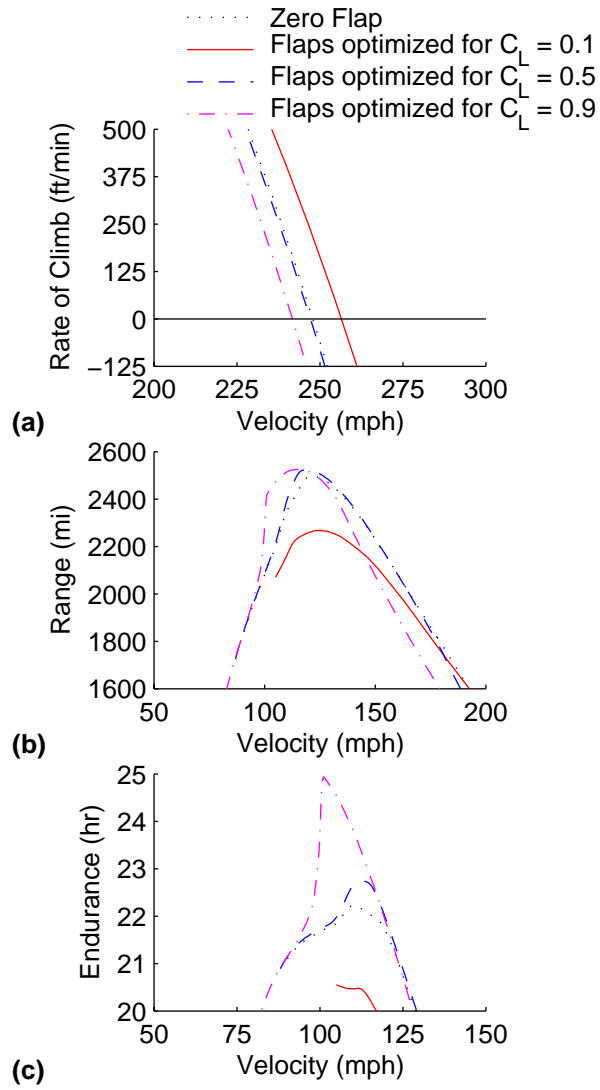


Figure 2.11: Examination of performance benefits: (a) maximum velocity, (b) range, and (c) endurance.

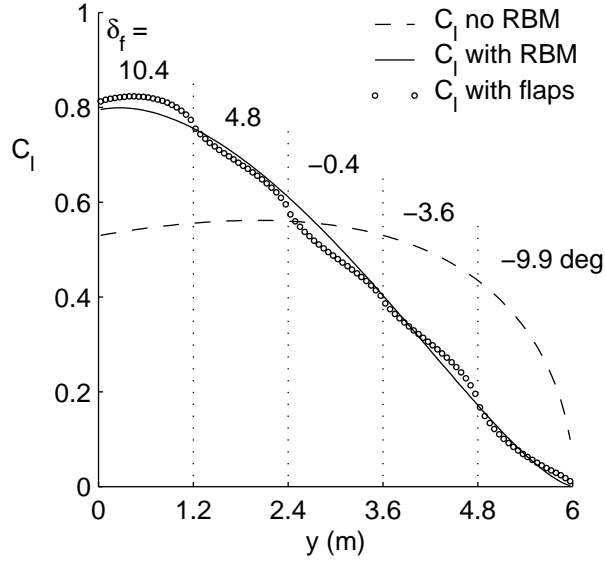


Figure 2.12: Calculated C_l distributions for $C_L = 0.5$: (i) optimal distribution with no RBM constraint, (ii) optimal distribution with RBM constraint, (iii) distribution calculated by WINGS with optimized flap angles.

flaps for RBM alleviation at high- g was explored. For this case, it was assumed that the aircraft was flying at $4.0g$, but the design wing RBM corresponded to that experienced by the wing at $3.0g$ when elliptically loaded. Therefore, the RBM constraint was prescribed to be 75% of the RBM for elliptical loading. The design C_L was chosen to be 0.5. Figure 2.12 shows the spanwise C_l distribution from the WINGS code using the flap angles predicted by the approach as marked. Also shown for comparison are the optimum C_l distributions for minimum induced drag with and without the RBM constraint.

It is to be noted that for high C_L and larger RBM alleviations, flap angles can be fairly large and could result in flow separation off the flap leading to reduced flap effectiveness. This reduced effectiveness has not been taken into consideration in the WINGS analysis. Additionally, the rigid wing assumption may not be correct, particularly at high dynamic pressures. These two factors need to be taken into consideration in a more refined version of the current approach. Nevertheless,

the results provide demonstration that the approach is successful in predicting the required flap-angle variation. The results also provide confidence that the multiple TE flaps are successful in relieving the RBM and can thus be used to design wings of lower weight.

2.3.2 Example 2: Nonplanar Wing

The second example uses the same wing planform as presented in Example 1, with the exception of a 90-degree winglet of height $0.1b$ added to the wing tip, as seen in Fig. 2.13. Although the chosen winglet may not be the best selection for the purposes of reducing induced drag, this example wing was chosen to simply illustrate the application of the approach to a nonplanar wing geometry.

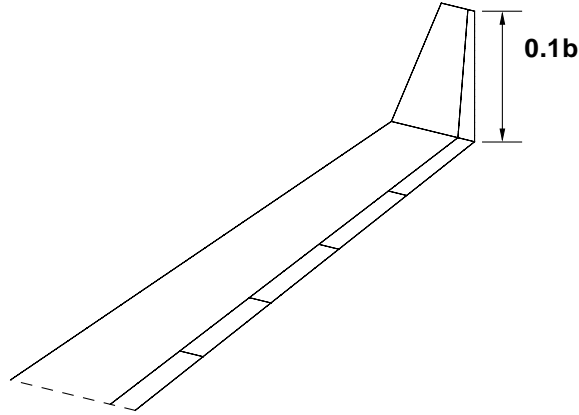


Figure 2.13: Wing and winglet geometry for Example 2.

The wing has five TE flaps on the planar portion and one flap on the winglet, with each flap having the same span and chord ratio of 0.2. The airfoil used for this example is the same as that used in Example 1, and is used for both the wing and the winglet. The flaps were set to the optimum angles, as determined by the current approach for a wing C_L of 0.5. Figure 2.14 shows the resulting C_l dis-

tribution with each control section drag polar and the corresponding flap angles. The drag polars along the wing were computed using XFOIL, with the planar portion of the wing operating at $Re\sqrt{C_l}$ of 3 million, and the drag polar from the winglet control section operating at a Reynolds number of 2.4 million. The optimum C_l distribution for minimum induced drag is also shown for reference. It can be seen that the optimum flap angles for this flight condition ensures not only that the each section C_l corresponds to a point inside the LDR, but also produces a C_l that closely matches the optimum C_l distribution for minimum induced drag. Therefore, the results demonstrate that the optimum flap-angle distribution achieves a loading that is close to that required for minimum induced drag, while supporting laminar flow over nearly the entire wing. Thus the approach is also effective in determining optimum C_l distributions and corresponding flap angles for a nonplanar wing.

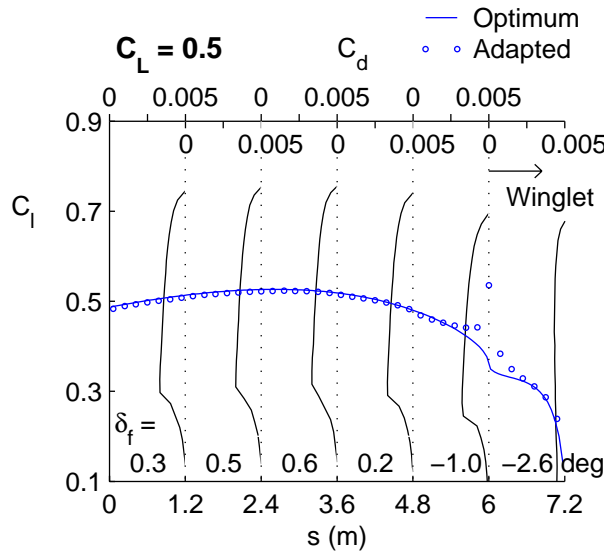


Figure 2.14: Spanwise C_l distributions and drag polars for flaps optimized for $C_L = 0.5$.

2.4 Summary

With the increasing interest in the use of variable spanwise camber for future adaptive wings, an approach was developed to determine optimum lift distributions at various flight conditions for a wing with multiple trailing-edge flaps. Using the concept of additional and basic lift distributions, and the understanding of the aerodynamics that bring about a minimum in profile drag and induced drag, it was possible to determine flap angles that produce the ideal lift distribution for a particular adaptation objective: minimization of drag, or minimization of drag with a wing root-bending moment constraint. In the current study, two example wings were examined: (1) a planar wing, and (2) a nonplanar wing. For both cases, a minimization of both induced and profile drag was achieved using the optimum flap angles as determined by the current approach for a wide range of wing lift coefficients. Examining the total wing drag coefficient as a function of the wing lift coefficient, it was seen that the optimum-flap schedule determined for a given wing lift coefficient results in the least drag at that specified lift coefficient, demonstrating the effectiveness of the current approach.

The performance benefits due to the optimum flap angles were also examined, and an increase in maximum velocity, maximum range, and maximum endurance were observed when compared to the zero-flap setting case. The trailing-edge flaps were also found to be successful in relieving root-bending moment when applying a root-bending moment constraint and using the optimized flap angles determined by the current approach.

Chapter 3

Ideal Aerodynamics of Ground-Effect and Formation Flight

Ground-effect and formation flight of aircraft is presented in this chapter as the second portion of the research, and as a second approach for aircraft drag reduction. With growing technology in the fields of adaptive aerodynamics, control of aircraft position, and precision measurement, there is an increasing interest in the use of formation flight and flight in ground-effect as alternative methods for drag reduction of future aircraft. Although the everyday use of these flight techniques is far from the present, the objective of the current study was to further investigate the aerodynamic benefits of formation flight and ground-effect flight, and in particular, the benefits of combined formation and ground-effect flight. Presented first in this chapter is the methodology of the numerical approaches developed, including an optimum-loading method as well as an exact approach for elliptically loaded wings both in ground effect (IGE) and out of ground effect (OGE). Presented next is the validation of the optimum-loading method, followed by a discussion of the results. The results from this study focus on three main topics: (1) the effect of lateral separation on the drag benefits for formations flying out of ground effect, (2) the benefits of combined formation and ground-effect flight,

and (3) the optimal vee shapes of formations. A summary of the study and its findings are given at the end of the chapter.

3.1 Methodology

This section will address the methodology of the numerical approaches developed for the current study. First presented is the procedure used to determine the optimum lift distribution for each wing in a formation, either in ground effect (IGE) or out of ground effect (OGE), which produces minimum formation induced drag. This section will also present the method used to simulate ground effect, as well as the details pertaining to the prescription of elliptical lift distributions. For elliptically loaded wings, the development of an exact approach is presented, which was used in the analysis of lateral separation between wings and its effect on formation induced drag. And lastly, the details of the approach used to determine the optimum vee-formation shape are given.

3.1.1 Optimum Lift Distribution for Minimum Induced Drag

To determine the optimum lift distribution on multiple wings in formation, the methodology of Frazier and Gopalarathnam²⁹ was used. The methodology was extended in the current study to handle nonplanar wings, each with an arbitrary spanwise variation of dihedral. The details of the numerical approach are similar to that presented in Chapter 2, Section 2.1.1, with the exception that multiple wings are taken into consideration, with constraints placed on the lift and rolling moment on each wing. Even so, for the sake of completeness, the methodology of the approach used in this study is presented in its entirety.

In this method, the calculus-of-variation approach of Jones⁴⁸ is first used to

determine the optimum downwash behind the wings. The wake is assumed to be rigid, inviscid, and invariant with the streamwise direction, and it is assumed to trail behind the wings in the direction of the freestream.

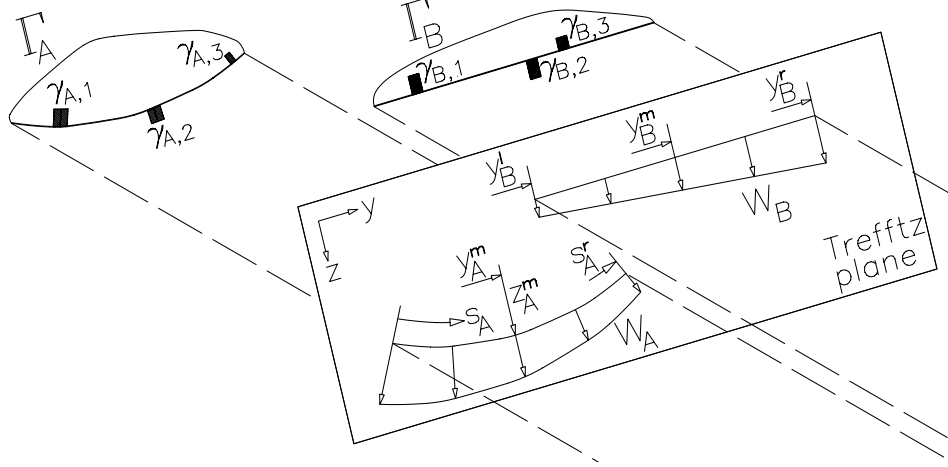


Figure 3.1: Illustration of the loading and Trefftz-plane normalwash for the two-wing example.

Figure 3.1 is an illustration of an example two-wing formation, where A is a non-planar wing with spanwise curvature, while B is a planar wing. The wings need not be identical but both are assumed to be optimally loaded. The lift distributions on the two wings are such that the total induced drag of the formation is a minimum, and the total lift on each wing equals the corresponding weight while the rolling moment for each wing is zero. The position along the curved wing A is denoted using the arc length s_A and the local dihedral angle at any spanwise location is $\theta_A(s_A)$. $\Gamma_A(s_A)$ and $\Gamma_B(s_B)$ are the bound-vorticity distributions associated with the original lift distributions on the two wings A and B. The lift L_A and L_B on each wing can be computed by spanwise integration, as shown in Eq. 3.1 for wing A.

$$L_A = \rho V_\infty \int_0^{s_A^r} \Gamma_A(s_A) \cos[\theta_A(s_A)] ds_A \quad (3.1)$$

The wing rolling moment R due to the lift distribution can also be computed from the Γ distribution, and is shown in Eq. 3.2 for wing A. The function $r_A(s_A)$, shown in Eq. 3.3, is the contribution to the rolling moment due to a unit load, acting normal to the curved wing at s_A .

$$R_A = -\rho V_\infty \int_0^{s_A^r} \Gamma_A(s_A) r_A(s_A) ds_A \quad (3.2)$$

$$r_A(s_A) = \cos[\theta_A(s_A)][y_A(s_A) - y_A^m] - \sin[\theta_A(s_A)][z_A(s_A) - z_A^m] \quad (3.3)$$

Using the Trefftz-plane normalwash distributions $w_A(s_A)$ and $w_B(s_B)$ shown in Fig. 3.1, the total induced drag of the entire formation with this lift distribution can be computed as shown in Eq. 3.4.

$$D = \frac{\rho}{2} \int_0^{s_A^r} w_A(s_A) \Gamma_A(s_A) ds_A + \frac{\rho}{2} \int_0^{s_B^r} w_B(s_B) \Gamma_B(s_B) ds_B \quad (3.4)$$

As pointed out in Ref. 28, the induced drag for each individual wing cannot be determined using the Trefftz-plane normalwash and has to be computed using a near-field method. Using wing A as an example, suppose the lift distribution on the wing is modeled using a bound vortex of varying strength $\Gamma_A(s_A)$ along the quarter-chord line and $\bar{w}_A(s_A)$ is the normalwash distribution along this line, then the induced drag of wing A is:

$$D_A = \rho \int_0^{s_A^r} \bar{w}_A(s_A) \Gamma_A(s_A) ds_A \quad (3.5)$$

It was shown by Iglesias and Mason²⁸ that when using a vortex lattice method (VLM), the bound vortex leg of each horse-shoe vortex needs to be unswept in order for the total near-field induced drag value from Eq. 3.5 to match that computed from the far-field integration using Eq. 3.4. For this reason, the bound-

vortex legs in the VLM formulation for the current work are unswept, as illustrated in Fig. 3.2. In addition, when modeling multiple lifting surfaces with overlapping wake traces using the VLM, care was taken in the current work to ensure that the overlapping trailing-vortex legs of the wings were exactly aligned, as shown in Fig. 3.2.

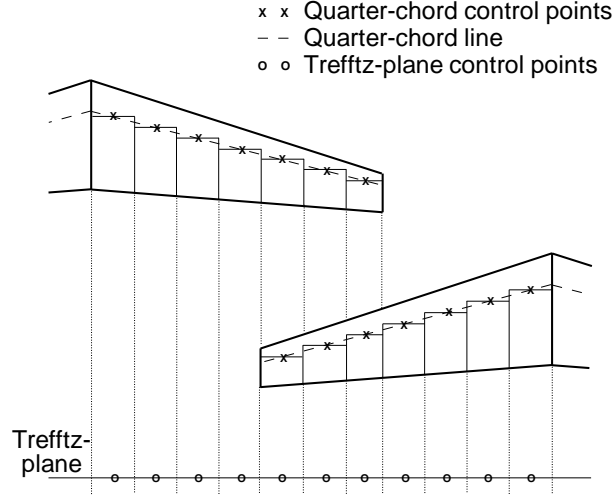


Figure 3.2: Illustration of vortex-lattice arrangement for a pair of swept wings.

The goal of the current method is to determine the downwash distribution behind the wings that will result in a minimum for the total induced drag of the entire system of wings while satisfying the constraints on the desired lift and desired zero rolling moment on each wing. As presented by Jones,⁴⁸ if the original lift distribution results in minimum induced drag, then a small variation in the shape of the lift distribution will produce no first-order change to the formation induced drag. The change in the formation induced drag due to a small variation in the Γ distribution (referred to as additional distribution) is composed of three parts:⁴⁸

1. The drag arising from the additional Γ distribution acting on the additional Trefftz-plane normalwash distribution
2. The drag arising from the original Γ distribution acting on the additional

Trefftz-plane normalwash distribution

3. The drag arising from the additional Γ distribution acting on the original Trefftz-plane normalwash distribution

The first part is a second-order term and can be neglected when compared to the other two parts. From Munk's mutual drag theorem,⁴⁹ the second and third parts of the additional induced drag are equal. Therefore, if the first-order change in formation induced drag is to be zero, then it is sufficient to set the drag arising from the additional Γ distribution acting on the original Trefftz-plane normalwash distribution (third part) to zero.

In order to satisfy the constraints on the specified lift and zero rolling moment, the additional Γ distribution should be selected such that it generates no additional lift or rolling moment for each wing. This additional Γ distribution is shown in Fig. 3.1 along with the original Γ distribution for the two wings. Using the arguments of Jones,⁴⁸ any additional distribution meeting these requirements can be subdivided into groups of three elements, so that each individual group independently satisfies the constraints. For instance, wing A has an additional distribution, which is composed of three elements having areas $\gamma_{A,1}$, $\gamma_{A,2}$, and $\gamma_{A,3}$, and are arbitrarily located at $s_{A,1}$, $s_{A,2}$, and $s_{A,3}$ respectively, as seen in Fig. 3.1. The additional Γ distribution must satisfy the following conditions: (i) there should be no change in the lift on wings A and B (Eqns. 3.6–3.7), (ii) there should be no change in the rolling moments (Eqns. 3.8–3.9), and (iii) there should be no change in the total induced drag (Eqn. 3.10). In Eq. 3.10, $w_{A,1}$, $w_{A,2}$, and similar terms are the Trefftz-plane normalwash values associated with the original Γ distribution at the corresponding locations $s_{A,1}$, $s_{A,2}$, and so on.

$$\gamma_{A,1} \cos[\theta_A(s_{A,1})] + \gamma_{A,2} \cos[\theta_A(s_{A,2})] + \gamma_{A,3} \cos[\theta_A(s_{A,3})] = 0 \quad (3.6)$$

$$\gamma_{B,1} \cos[\theta_B(s_{B,1})] + \gamma_{B,2} \cos[\theta_B(s_{B,2})] + \gamma_{B,3} \cos[\theta_B(s_{B,3})] = 0 \quad (3.7)$$

$$\gamma_{A,1} r_A(s_{A,1}) + \gamma_{A,2} r_A(s_{A,2}) + \gamma_{A,3} r_A(s_{A,3}) = 0 \quad (3.8)$$

$$\gamma_{B,1} r_B(s_{B,1}) + \gamma_{B,2} r_B(s_{B,2}) + \gamma_{B,3} r_B(s_{B,3}) = 0 \quad (3.9)$$

$$\gamma_{A,1} w_{A,1} + \gamma_{A,2} w_{A,2} + \gamma_{A,3} w_{A,3} + \gamma_{B,1} w_{B,1} + \gamma_{B,2} w_{B,2} + \gamma_{B,3} w_{B,3} = 0 \quad (3.10)$$

It can be seen that in order to satisfy Eqs. 3.6–3.10, the Trefftz-plane normalwash along the wake traces of each wing must be of the form $w_A(s_A) = P_A \cos[\theta_A(s_A)] + Q_A r_A(s_A)$ and $w_B(s_B) = P_B \cos[\theta_B(s_B)] + Q_B r_B(s_B)$, where P_A , Q_A , P_B , and Q_B are constants that are determined using the specified values of the lift, L_A and L_B , and the rolling moments, R_A and R_B , for the two wings. In the current problem, R_A and R_B are both zero. For a planar wing ($\theta = 0$), this normalwash variation simplifies to a linear spanwise variation²⁹ of the downwash distribution, $w_B(y) = P_B + Q_B(y - y_B^m)$, as illustrated for wing B in Fig. 3.1. Although this method has been illustrated using two wings, the result can be generalized for any arbitrary number of wings in formation flight.

The optimum-downwash formulation for planar wings is valid only for formation geometries in which the wake traces of the wings in the Trefftz-plane do not intersect or overlap with each other. If any two planar wings have intersecting or overlapping wake traces, then they share the same Trefftz-plane downwash values at each of the common points of overlap. Because the formulation does not account for such a constraint in the downwash, the method is restricted to wings

that do not intersect or overlap in the front view. This limitation is also applicable to the constrained-minimization approach of Ref. 28.

The Γ distributions on the wings and the associated Trefftz-plane downwash distributions, w , behind them are closely related and can be determined using a discrete-vortex method similar to that described by Blackwell.⁵⁰ Briefly, the bound vorticity distribution on all of the wings and the trailing vorticity shed behind them are approximated using n horseshoe vortices, each having a constant value for the bound vortex strength Γ . With such a formulation, the n -dimensional $\mathbf{\Gamma}$ vector and the n -dimensional \mathbf{w} vector can be related using an $n \times n$ influence coefficient matrix \mathbf{I} as shown in Eq. 3.11. For a known \mathbf{w} , the $\mathbf{\Gamma}$ distribution can be computed by solving Eq. 3.11 and the lift, rolling moment, and drag can then be determined using Eqs. 3.1–3.5.

$$\mathbf{I} \cdot \mathbf{\Gamma} = \mathbf{w} \quad (3.11)$$

For the current problem, $w(y)$ for each wing is known in terms of the two unknown constants P and Q . These unknowns are computed using a single step of Newton’s method as shown in Eq. 3.12 for the two-wing example used earlier in this section. The solution is made simple because of the fact that zero values for P and Q correspond to zero values for L and R . The Jacobian of partial derivatives is computed using finite differencing. For example, $\partial L_A / \partial P_A$ is computed by making a small change to P_A and computing the change to L_A . The right hand side is a vector of the desired values of lift, L_A and L_B , and rolling moments, R_A and R_B . In the current problem, the rolling moments are set to zero. Thus the P and Q can be determined using Eq. 3.12. This approach can be readily extended to a formation of more than two wings.

$$\begin{pmatrix} \frac{\partial L_A}{\partial P_A} & \frac{\partial L_A}{\partial Q_A} & \frac{\partial L_A}{\partial P_B} & \frac{\partial L_A}{\partial Q_B} \\ \frac{\partial R_A}{\partial P_A} & \frac{\partial R_A}{\partial Q_A} & \frac{\partial R_A}{\partial P_B} & \frac{\partial R_A}{\partial Q_B} \\ \frac{\partial L_B}{\partial P_A} & \frac{\partial L_B}{\partial Q_A} & \frac{\partial L_B}{\partial P_B} & \frac{\partial L_B}{\partial Q_B} \\ \frac{\partial R_B}{\partial P_A} & \frac{\partial R_B}{\partial Q_A} & \frac{\partial R_B}{\partial P_B} & \frac{\partial R_B}{\partial Q_B} \end{pmatrix} \begin{pmatrix} P_A \\ Q_A \\ P_B \\ Q_B \end{pmatrix} = \begin{pmatrix} L_A \\ R_A \\ L_B \\ R_B \end{pmatrix} \quad (3.12)$$

For a given formation of several wings with the geometry specified in the front view, known values for the specified lift, and zero rolling moments, the approach thus allows for the computation of the P and Q that in turn determine the Trefftz-plane downwash. The Γ distributions are then computed, from which other quantities can be determined. If in addition, the planform geometry of the entire formation is known, the induced drag for each individual wing can also be computed using the near-field approach²⁸ shown in Eq. 3.5 for wing A .

3.1.2 Ground Effect

For analysis of a single wing or a formation of several wings in ground effect, an additional formation is modeled as a mirror image under the ground plane. The wings in the mirrored formation are specified to have values of lift that are negative and equal to those specified for the corresponding wings in the upper formation, as illustrated in Fig. 3.3 for a two-wing formation in ground effect. As an example, for wing, A , in ground effect, at a height above ground of h_A , the wing mirrored underneath, designated A_m , would have the desired value of lift $L_{Am} = -L_A$. The desired rolling moments, R_A and R_{Am} , remain zero. Beyond these changes, the formulation for calculating the optimum normalwash and lift distributions remains the same as that presented for flight out of ground effect. In the vortex-lattice implementation, lateral symmetry as well as symmetry about the ground plane

are used to significantly reduce the computational time, as explained in greater detail in Appendix A.

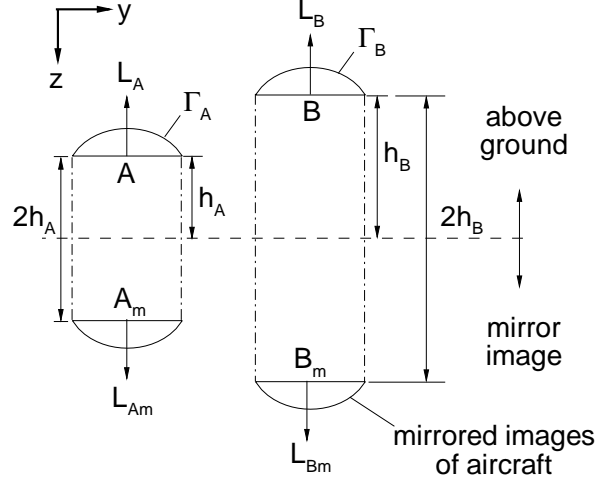


Figure 3.3: Model of two-wing formation in ground effect.

3.1.3 Prescribed Elliptical Lift Distribution

While the optimum lift distribution for a given formation results in the minimum total induced drag, it is desirable to determine how sensitive the induced drag is to deviations of the lift distribution from the optimum distribution. For this purpose, formations of planar wings were also examined in which each wing was assumed to have an elliptical spanwise lift distribution. When an elliptical loading is prescribed, the wing rolling-moment constraint is automatically satisfied. Prescription of an elliptical loading also enables the investigation of formation geometries with overlapping wings, which is not feasible with optimally-loaded wings. More importantly, the exact solution for the cross-flow velocity in the Trefftz plane is known for an elliptically-loaded wing. This cross-flow velocity can be used to obtain the exact solution for the total drag of a formation of several wings flying in ground effect (IGE) or out of ground effect (OGE). The exact solution

can also serve to validate the vortex-lattice solutions for elliptically-loaded wings.

For a wing with its plane of symmetry located at y^m , the prescribed elliptical lift distribution results in an elliptical Γ distribution over the span as follows:

$$\frac{\Gamma(y, y^m)}{V_\infty} = \frac{\Gamma_0}{V_\infty} \sqrt{1 - \left[\frac{2(y - y^m)}{b} \right]^2} \quad (3.13)$$

where,

$$\frac{\Gamma_0}{V_\infty} = \frac{4L}{\pi \rho b V_\infty^2} = \frac{2SC_L}{\pi b} \quad (3.14)$$

When using the vortex-lattice implementation, the vortex strengths are determined from the elliptical loading of lift on each wing. These vortex strengths are used to compute the resulting Trefftz-plane downwash, the induced drag of the formation (Eq. 3.4), and induced drag values of individual wings (Eq. 3.5). For a single elliptically-loaded wing operating out of ground effect, lifting line theory gives the induced drag to be:

$$D_{ell} = \frac{2}{\pi \rho V_\infty^2} \left(\frac{L}{b} \right)^2 \quad (3.15)$$

The exact solution for the cross-flow velocity distribution in the Trefftz plane, expressed using complex variables, is:^{66,67}

$$\frac{W(y, z)}{V_\infty} = \frac{v - iw}{V_\infty} = i \frac{w_0}{V_\infty} \left[\frac{\mathcal{Z}}{\sqrt{\mathcal{Z}^2 - (b/2)^2}} - 1 \right] \quad (3.16)$$

where $\mathcal{Z} = y + iz$ is the complex coordinate in the Trefftz plane with the origin at the mid-span location of the wake trace of the wing. The Trefftz-plane downwash at the mid-span location on the wake trace, w_0 , is given by:

$$\frac{w_0}{V_\infty} = \frac{4L}{\pi \rho V_\infty^2 b^2} = \frac{2C_L}{\pi AR} \quad (3.17)$$

The downwash, w , and the vertical coordinate, z , are assumed to be positive in the downward direction. For planar wings, only the downwash component of $W(y, z)$ is of interest and is given by:

$$\frac{w(y, z)}{V_\infty} = \frac{w_0}{V_\infty} \Re \left[1 - \frac{\mathcal{Z}}{\sqrt{\mathcal{Z}^2 - (b/2)^2}} \right] \quad (3.18)$$

where the symbol \Re denotes the real part of a complex variable. Figure 3.4 shows the variations of $w(y/b)/w_0$ for various values of z/b . It can be seen that for $z = 0$, the downwash is constant over the span and there is upwash outboard of the wing tip. Immediately outboard of the wing tip, there is a singularity as the upwash goes to infinity. As a result of this singularity, evaluation of the induced drag for overlapping wings needs to be done carefully.

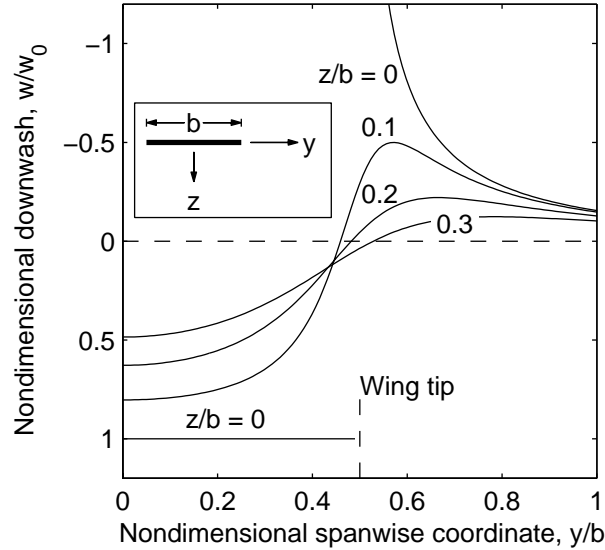


Figure 3.4: Variation with y/b for various z/b of the downwash in the Trefftz plane for an elliptically-loaded wing. Inset shows wake trace and coordinate system.

For a formation of several elliptically-loaded wings of equal span and lift, in or out of ground effect, the exact solution for the total induced drag can be developed using the interference drag of a two-wing formation. This two-wing interference drag can be obtained in a manner similar to that for Prandtl's biplane theory.⁶⁸

Figure 3.5(a) shows two elliptically-loaded wings, A and B, which have the same span and lift. The streamlines of the Trefftz-plane cross-flow velocity distribution, $W(y, z)$, of wing A are also plotted in Fig. 3.5(a) for reference. The total induced drag, $D_2(Y_2, Z_2)$, for the two-wing formation as a function of the lateral separation, Y_2 , and vertical separation, Z_2 , and can be written as the sum of the self-induced contributions, D_{AA} and D_{BB} , and the mutual-interference contributions D_{AB} and D_{BA} . Each self-induced drag term is equal to the drag of a single elliptically-loaded wing, D_{ell} . The two mutual interference contributions, D_{AB} and D_{BA} , are equal and are denoted by D_{int} .

$$D_2(Y_2, Z_2) = 2D_{ell} + 2D_{int}(Y_2, Z_2) \quad (3.19)$$

The self-induced drag terms can be determined using Eq. 3.15, and the mutual-interference term, D_{int} , can be computed for cases with non-overlapping wake traces by integrating over the wake trace of wing B as follows:

$$D_{int}(Y_2, Z_2) = \frac{\rho}{2} \int_{Y_2-b/2}^{Y_2+b/2} w_A(y, Z_2) \Gamma_B(y, Y_2) dy \quad (3.20)$$

where, Γ_B is the bound circulation distribution on wing B obtained by setting $y_m = Y_2$ in Eq. 3.13 and w_A is the downwash distribution due to wing A obtained by setting $z = Z_2$ in Eq. 3.16. For cases with overlapping wake traces ($Z_2 = 0$ and $0 < Y_2 < b$), the singularity of infinite upwash in w_A just outboard of the wing tip was handled by evaluating the Cauchy Principal Value at the singularity as follows:

$$D_{int}(Y_2, Z_2) = \frac{\rho}{2} \lim_{\epsilon \rightarrow 0} \left(\int_{Y_2-b/2}^{b/2-\epsilon} w_A \Gamma_B dy + \int_{b/2+\epsilon}^{Y_2+b/2} w_A \Gamma_B dy \right) \quad (3.21)$$

The expressions for equations 3.20 and 3.21 were solved using the Matlab

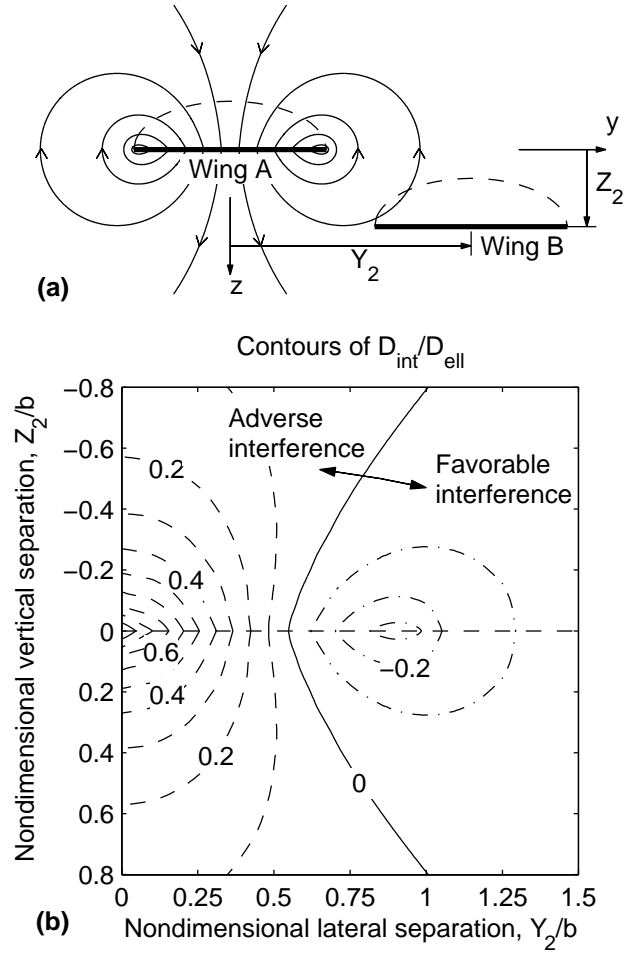


Figure 3.5: A pair of elliptically loaded wings, A and B: (a) illustration of the wake-trace geometry, with the streamlines shown for wing A, and (b) contours of D_{int}/D_{ell} as a function of Y_2/b and Z_2/b .

Symbolic Toolbox.⁶⁹ It can be shown that the nondimensional interference drag, D_{int}/D_{ell} , is a function of only the nondimensional lateral separation, Y_2/b , and vertical separation, Z_2/b . Figure 3.5(b) shows the contours of D_{int}/D_{ell} as a function of Y_2/b and Z_2/b . Negative D_{int} is termed “favorable interference” as it results in a lower total drag for the formation, while positive D_{int} is considered “adverse interference.” When wing A has positive lift and wing B has negative lift, as it would be if B were the mirror image of another wing flying close to the ground, then the interference drag between A and B would have the same magnitude, but would change sign. Therefore, regions of favorable interference become adverse interference and vice versa when wings A and B have lift acting in opposite directions.

It can be seen from Fig. 3.5(b) that the favorable interference is maximum at $Z_2/b = 0$ and $Y_2/b = 0.91$. That is, the maximum favorable interference occurs when the two wings have a small lateral overlap of approximately 9% of the wing span. When there is lateral overlap, the extreme-left portion of wing B that is overlapped laterally with wing A will experience the Trefftz-plane downwash of wing A. This downwash acting on the Γ of the overlapped portion of wing B will contribute to an increase in total induced drag. However, the spanwise portion of wing B that is just outboard of wing A will experience the significant Trefftz-plane upwash of wing A. This upwash acting on the Γ of the portion of wing B that is just outboard of wing A will contribute to a decrease in the total induced drag. These two contributions change with changes to the lateral separation, such that the small lateral overlap of 9%-span results in maximum favorable interference.

To demonstrate how the two-wing interference-drag solution can be used to determine the total induced drag of several wings flying in formation, IGE or OGE, a formation of N elliptically-loaded wings, numbered 1 to N , is considered. For the case of combined formation and ground-effect flight, the total formation

drag can be written as:

$$D = \sum_{j=1}^N \sum_{i=1}^N D_{ij} + \sum_{j=1}^N \sum_{i=1}^N D_{i(j_m)} \quad (3.22)$$

The first term of Eq. 3.22 provides the total drag of the formation when flying OGE. When $i = j$, D_{ij} is equal to D_{ell} . The second term provides the additional contribution due to ground effect, with $D_{i(j_m)}$ being the induced drag due to the downwash field of the image, j_m , of wing j acting on the wing i . It is also seen that each of the terms of D_{ij} and $D_{i(j_m)}$ can be computed using the two-wing interference-drag solution $D_{int}(Y_2, Z_2)$. For the special case of a formation of N elliptically-loaded planar wings that are flying with uniform lateral separation between any two adjacent wings, zero vertical separation, and close to the ground, the total induced drag can be written as:

$$D = ND_{ell} + D_{ff} + D_{ge} \quad (3.23)$$

where D_{ff} is the interference drag of the entire formation OGE and D_{ge} is the interference drag due to ground proximity. D_{ff} can be written as:

$$D_{ff} = \sum_{f=1}^{(N-1)} 2f D_{int}[(N-f)Y, 0] \quad (3.24)$$

where Y is the uniform lateral spacing between any two adjacent wings in the formation, with zero vertical separation. D_{ge} can be written as:

$$D_{ge} = -ND_{int}(0, 2h) - \sum_{g=1}^{(N-1)} 2g D_{int}[(N-g)Y, 2h] \quad (3.25)$$

where h represents the height of the formation above ground.

This formulation allows for the decomposition of the total induced drag into different contributions. In Eq. 3.24, the term for $f = N - 1$ represents the contri-

butions of the interference drag between the $N - 1$ pairs of adjacent wings (wings i and $i + 1$), the term for $f = N - 2$ represents the contributions of the interference drag between the $N - 2$ pairs formed by a wing and its next-to-immediate neighbor (wings i and $i + 2$), and so on. Similarly in Eq. 3.25, the first term represents the N contributions of the interference drag between a wing and its own image, the $g = N - 1$ represents the $N - 1$ contributions of the interference drag between a wing and the image of its adjacent neighbor (wings i and image of $i + 1$), and so on. As shown later, this decomposition makes it possible to explain certain patterns in the variation of drag with lateral spacing and ground height. Finally, it is to be noted that this exact formulation can only provide the total induced drag and cannot provide the drag of each individual in a formation. When the drag of each individual is needed, the vortex-lattice implementation is used.

3.1.4 Optimum Vee-Formation Shape

It is well known that a number of species of migrating birds such as swan, geese, and cranes fly in typical vee-shaped formations. This flight mode is shown to result in an aerodynamic benefit for all individuals.⁹⁻¹² From Munk's stagger theorem,⁴⁹ any lifting assemblage may be staggered, or displaced in the direction of motion, without changing the total induced drag. To determine optimal vee formations, a Newton iteration scheme was developed to determine the streamwise locations that result in equal induced drag for all the individuals. At each step of the Newton iteration, the matrix equation

$$\mathbf{J} \cdot \delta \mathbf{x} = -\mathbf{F} \quad (3.26)$$

is solved. In this equation, \mathbf{F} is the vector containing the residuals of the functions to be zeroed, \mathbf{J} is the Jacobian matrix that contains the gradient information, and

$\delta \mathbf{x}$ contains the corrections to the design variables causing \mathbf{F} to approach zero. The target induced drag for each individual, D_{target} , is simply the total induced drag of the formation calculated in the Trefftz plane divided by the total number of wings, N . The residual vector \mathbf{F} is the difference between the current induced drag for each wing, determined using the vortex-lattice implementation, and the D_{target} . The Jacobian matrix contains the partial derivatives of the values of individual induced drag with respect to the streamwise locations of the wings and is determined using finite differencing.

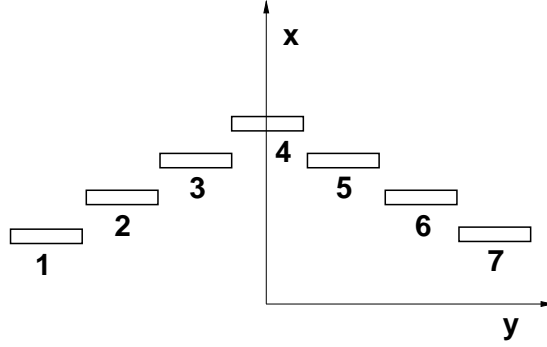


Figure 3.6: Numbering for a seven-wing vee formation.

For each iteration, the matrix equation, Eq. 3.26, is solved to determine the vector $\delta \mathbf{x}$, as \mathbf{J} and \mathbf{F} are known. The resulting vector $\delta \mathbf{x}$, containing the corrections to the streamwise locations of the wings, is used for updating the shape of the vee formation. It was necessary to add an under-relaxation factor of 0.1 to make the iteration converge. That is, the x -location for wing j is updated as $x_j^{new} = x_j^{old} + (0.1)\delta x_j$. New individual induced drag values are then calculated using the updated streamwise locations and the residuals and Jacobian matrix are recalculated. This process is continued until the residuals are brought to within a given tolerance of zero, resulting in the streamwise locations for an optimum vee formation. Eqn. 3.27 shows the Jacobian \mathbf{J} , residual \mathbf{F} and the correction vector $\delta \mathbf{x}$ for a seven-wing formation as shown in Fig. 3.6. Symmetry is used to reduce

the computational time, hence only the right-hand side of the vee formation is altered to determine the optimal vee formation. The lead wing, or center wing, is not included in the formulation, as it is used as the reference wing.

$$\begin{pmatrix} \frac{\partial D_5}{\partial x_5} & \frac{\partial D_5}{\partial x_6} & \frac{\partial D_5}{\partial x_7} \\ \frac{\partial D_6}{\partial x_5} & \frac{\partial D_6}{\partial x_6} & \frac{\partial D_6}{\partial x_7} \\ \frac{\partial D_7}{\partial x_5} & \frac{\partial D_7}{\partial x_6} & \frac{\partial D_7}{\partial x_7} \end{pmatrix} \begin{pmatrix} \delta x_5 \\ \delta x_6 \\ \delta x_7 \end{pmatrix} = - \begin{pmatrix} D_5 - D_{target} \\ D_6 - D_{target} \\ D_7 - D_{target} \end{pmatrix} \quad (3.27)$$

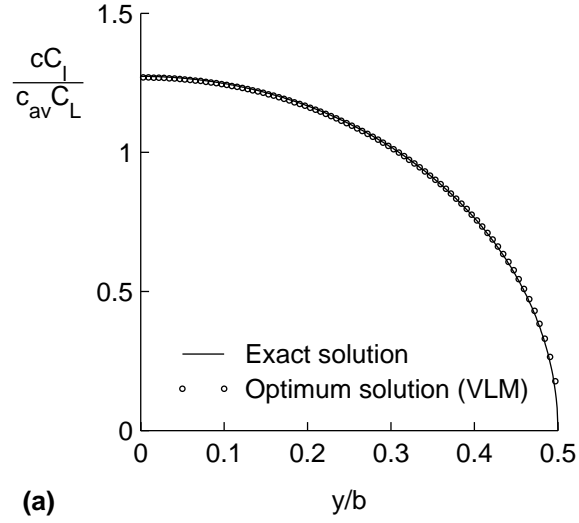
3.2 Validation of Optimum-Loading Method

This section presents a comparison of induced drag computed from the current optimum-loading VLM with exact solutions for wing formations IGE and OGE.

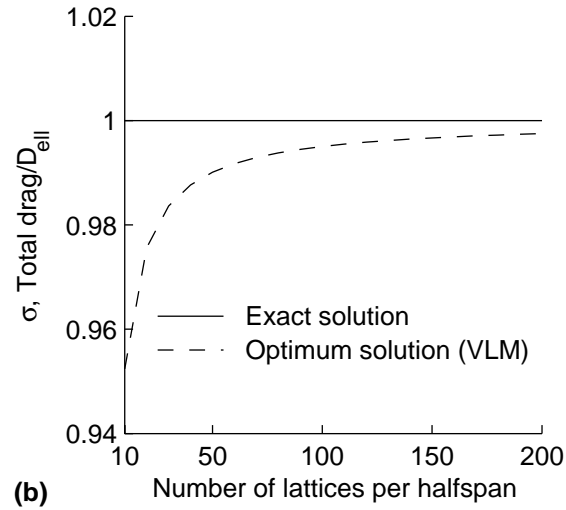
3.2.1 Planar Wing Out of Ground Effect

From classical lifting-line theory, the exact optimum lift distribution for a single planar wing flying OGE is an elliptical loading and the corresponding minimum induced drag is D_{ell} . Figure 3.7(a) shows a comparison of the lift distribution from the current method with the exact elliptical loading. The comparison is seen to be excellent. Figure 3.7(b) shows the convergence of the induced drag from the current method with increasing number of vortex lattices. It can be seen that the predicted drag converges toward the exact value with increasing number of lattices. For the current work, 80 lattices per half span of each wing have been used for all vortex-lattice computations in order to achieve a reasonable compromise between accuracy and computation time for the larger formation geometries.

The optimum loading for minimum induced drag was also computed for a symmetric formation of three wings and was compared with the results from the constrained-minimization approach of Iglesias and Mason.²⁸ Results obtained



(a)



(b)

Figure 3.7: Comparison of the optimal solution for a planar wing from VLM with the exact solution: (a) spanload distribution and (b) convergence of the predicted induced drag with increasing number of lattices per half span.

from the current method for the loading, the total induced drag and the drag of the individual wings are all identical to those presented by Iglesias and Mason.²⁸ The details of this comparison can be found in Ref. 29.

3.2.2 Single Wing in Ground Effect

Ashill¹⁹ has presented an exact approach for determining the minimum induced drag of wings in ground effect. The resulting induced-drag ratios for a planar and a nonplanar wing, as calculated by the current vortex-lattice method, have been compared with Ashill's exact results. The induced drag ratio, σ , is the ratio of the induced drag in ground effect nondimensionalized by D_{ell} for the same lift, span, and dynamic pressure. Thus, a lower value of σ indicates a larger ground-effect benefit for the wing. Figure 3.8 shows a comparison of the σ computed using the current method for optimally-loaded wings at various heights above ground with those from Ashill.¹⁹ The nonplanar wing used in this comparison has a 10%-span downward-pointing winglet at each wing tip. The agreement is seen to be excellent. The results also indicate that for a given h , a wing with a downward-pointing winglet experiences greater ground-effect benefits than a planar wing.

Also presented in Fig. 3.8 are the values of σ for the elliptically-loaded planar wing, determined using the exact solution of D_{int} in Fig. 3.5(b) and Eq. 3.23. As seen, the elliptically-loaded planar wing has nearly the same induced drag as an optimally-loaded planar wing at a given height above ground. This observation is not new; a similar comparison was presented by Ashill¹⁹ in which the minimum-induced drag results were compared with the induced drag computed by Weiselsberger¹⁷ for elliptically-loaded wings in ground effect.

The optimum normalwash and optimum lift distributions, for both planar and nonplanar wings, are presented in Fig. 3.9 for various values of h . Figure 3.9(a) shows the optimum Trefftz-plane downwash distributions for the planar wing of

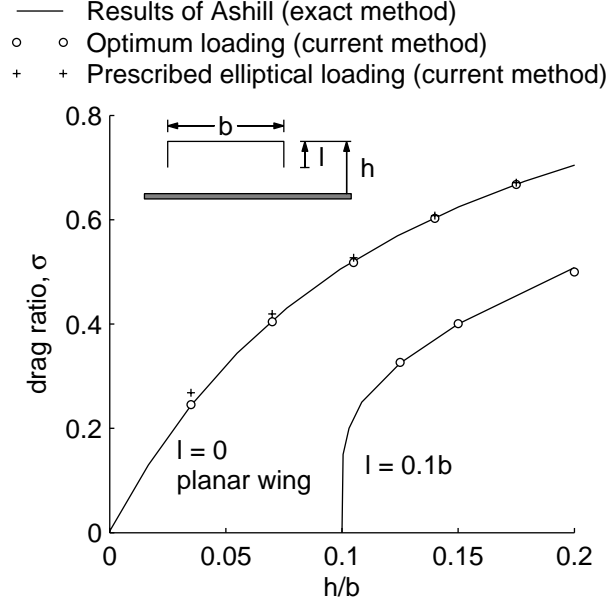


Figure 3.8: Comparison of drag factors for wings in ground effect from the current method with exact solutions from Ashill.

aspect ratio 8 and Fig. 3.9(b) shows the corresponding lift distributions. The $h/b = 0.02$ case is used to illustrate an example with extreme ground effect. The resulting lift distributions agree well with the results of de Haller,¹⁸ who showed that when the height above ground diminishes from infinity to zero, the optimal loading changes from elliptic to parabolic. Rozhdestvensky²⁰ found the same parabolic spanwise distribution for the optimal wing in extreme ground effect (clearances of 10% of the wing span or smaller).

The optimum normalwash distributions for the nonplanar wing, plotted in Fig. 3.9(c) as a function of the wing arc length, show that the normalwash on the winglet is exactly zero. Because of the presence of the winglet, however, the downwash on the planar portion of the wing, at a given h , is less than the downwash on the wing without a winglet. This reduced downwash due to the winglet results in lower induced drag for the nonplanar wing when compared to a planar wing. The optimum load distributions for the nonplanar wing are presented in Fig. 3.9(d). It is seen that with changes in h there is hardly any change to the

loading on the planar portion as the changes are confined mainly to the loading on the winglet. For a wing designed to operate in ground effect at a given σ , a wing with a downward-pointing winglet may prove to be advantageous because the height of the planar portion of the wing above ground is greater than that for a wing without a winglet.

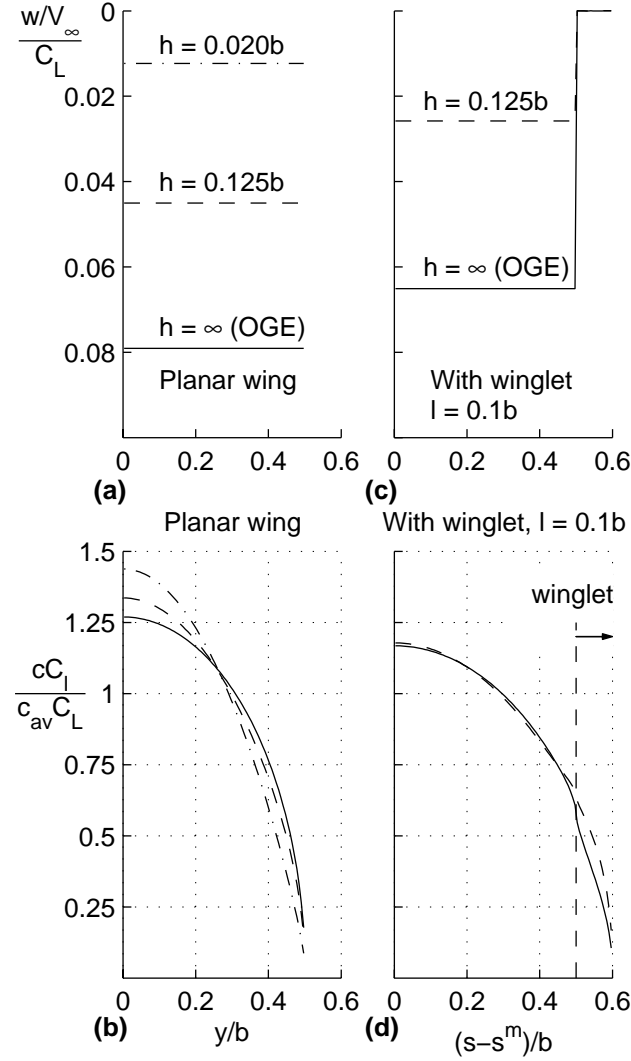


Figure 3.9: Planar and nonplanar wings in ground effect at various h : (a) Trefftz-plane downwash distributions for planar wings, (b) spanload distributions for planar wings, (c) Trefftz-plane normalwash distributions for nonplanar wings, and (d) spanload distributions for nonplanar wings.

Because flight safety becomes an increasingly important issue for small ground

clearances, it is desirable to develop concepts for achieving ground-effect benefits at larger clearances. It can be seen from Fig. 3.8 that for optimally-loaded and elliptically-loaded planar wings, the ground-effect benefit depends on h/b . It can be deduced from these results that for achieving a given ground-effect benefit, as determined by σ , a larger-span wing can fly at a larger ground clearance h than a smaller-span wing. For example, a 50% induced-drag savings can be achieved by flying at a height of approximately 10% of the wing span above the ground. Routine flight operations at this h/b can be dangerous for a 10-m span aircraft, but starts to become conceivable for a 100-m span aircraft concept.

3.3 Results

The results presented in this section focus on three main topics: (1) the effect of lateral separation on drag benefits for formations flying OGE, (2) the benefits of combined formation and ground-effect flight, and (3) the optimal vee shapes of formations. In all cases, the wings within a given formation are all assumed to be planar with identical span b , and supporting the same lift L . In the discussion of drag benefits, a comparison is made between drag ratios of different formations. For an N -wing configuration, IGE or OGE, the drag ratio, σ , is the ratio of total induced drag of that configuration to the induced drag of N elliptically-loaded planar wings of span b , with lift L , and flying in isolation OGE at the same freestream dynamic pressure as the formation.

3.3.1 Effect of Lateral Separation

To analyze the effects of lateral separation on formation flight, a formation of two planar wings is used. The vertical separation, Z , is assumed to be zero so that the two wings lie in the same horizontal plane. Two loading cases are considered:

one in which each wing is loaded optimally for minimum total induced drag, and the second in which each wing has a prescribed elliptical loading.

The variation of the drag ratio, σ , for this two-wing formation as a function of nondimensional lateral separation, Y/b , is shown in Fig. 3.10(a) for both the two loading cases. The results for the elliptical loading are shown from the vortex-lattice approach as well as from the exact approach, and these two approaches give nearly identical results. The results for the optimal-loading case are presented only for $Y/b > 1$ as the optimum-downwash theory, as presented earlier in this dissertation, is not valid for computing the minimum-induced-drag loading on planar wings with overlapping or intersecting wake traces. For $Y/b > 1$, a comparison of the induced-drag-ratio variations for the two loading cases illustrates that a formation of elliptically-loaded wings has virtually the same induced drag as a formation that has the theoretical optimum loading. This observation, made earlier by Lissaman and Shollenberger,¹⁰ has an important consequence for adaptive wings that can reconfigure their geometries (such as spanwise twist or camber distribution) for formation flight. The wing geometries can be adapted to achieve an elliptical loading that is invariant with formation geometry instead of an optimal loading that will need to be recomputed depending on the formation geometry.

It is seen from Fig. 3.10(a) that for values of lateral separation ($Y/b \gg 1$), the drag ratio asymptotes to 1 because the wings have little influence on each other. For $Y/b = 1$, corresponding to zero lateral overlap, the drag ratio is 0.73, representing a 27% drag reduction when compared to the total drag of two wings flying in isolation. As the lateral separation is decreased, the drag ratio continues to decrease until a minimum in the drag ratio is reached for a lateral separation of Y/b of 0.91 that corresponds to a geometry where there is a 9%-span lateral overlap of the wing tips. For this optimum lateral separation, the drag ratio is

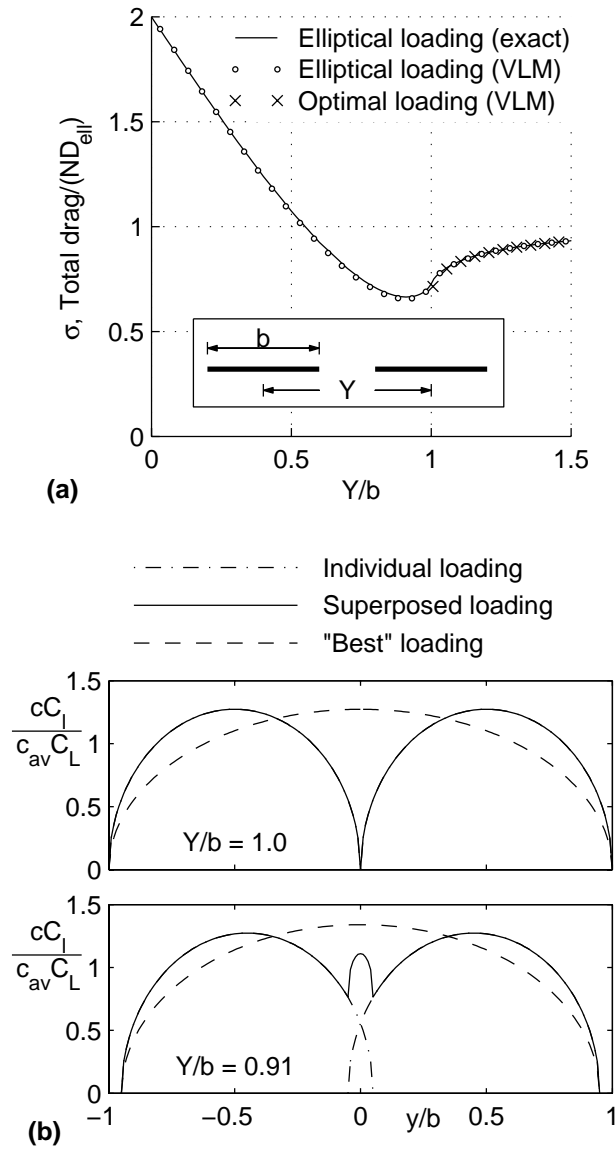


Figure 3.10: Two-wing formation: (a) variation of the formation drag ratio with lateral separation for optimal and elliptical loadings, with insets showing the wake traces, and (b) comparison of the superposed loading with the “best” loading for $Y/b = 1$ and $Y/b = 0.91$.

0.66, which represents a 44% reduction in drag when compared to the total drag of two wings flying in isolation.

The reason for the optimum lateral separation of $Y/b = 0.91$ can be deduced from a comparison of the loadings for $Y/b = 1$ and $Y/b = 0.91$ with the corresponding “best” loadings in Fig. 3.10(b). For any Y/b , the “best” loading is one that distributes the total formation lift elliptically over the formation span. The formation span is the lateral distance from the left wing tip of the left wing to the right wing tip of the right wing. For $Y/b = 1$ and $Y/b = 0.91$, the formation spans are $2b$ and $1.91b$ respectively. Although the formation span for $Y/b = 0.91$ is less than that for $Y/b = 1$, the superposed loading is closer to the “best” loading for $Y/b = 0.91$ than for $Y/b = 1$. For $Y/b < 0.91$ (not shown), the superposed loading is even closer to the corresponding “best” loading, but the formation span is also much smaller than for $Y/b = 0.91$. As a result of this tradeoff, $Y/b = 0.91$ is the optimum lateral separation.

It is also possible to quantify the formation drag benefit by determining an effective span for the formation. This effective span, b_{eff} , is the span of a single elliptically-loaded wing carrying the same total lift as the formation and having the same total induced drag as the formation. It can be shown that $b_{eff}/b = \sqrt{N/\sigma}$. For $Y/b = 0.91$, the effective span for this formation geometry is $1.73b$, implying that this two-wing formation at the optimum lateral separation behaves like a single large wing of span $1.73b$ with respect to induced-drag characteristics. For lateral separations much less than $Y/b = 0.91$, the drag ratio increases rapidly and reaches a value of 2 for $Y/b = 0$, which represents a 100% increase in the drag when compared to the total drag of two wings flying in isolation.

The 9%-span optimum lateral overlap of wing tips predicted in the current work for elliptically-loaded wings is close to those seen in wind-tunnel and flight experiments. Blake and Gingras³¹ presented wind-tunnel test results for two

delta-wing aircraft in formation, and compared wind-tunnel measurements with predictions from a vortex lattice method. Both predictions and the experimental measurements showed a trend of maximum drag reduction when there is an approximate 10–20%-span lateral overlap of wing tips in the formation. Recent experiments performed at NASA Dryden Flight Research Center^{33,34} analyzed performance benefits resulting from formation flight, using two modified F/A-18 aircraft. A summary of drag-reduction results computed using actual test points shows a maximum reduction in induced drag when there is an 8%–18%-span lateral overlap in wingtips, and a small vertical separation of approximately 5% of the wing span.³⁴ Given that the theoretical model in the current work does not account for wake rollup and assumes an elliptical loading, the results for the optimum lateral overlap agree well with the trends seen in the experiments.

3.3.2 Combined Formation and Ground-Effect Flight

The motivation for studying the benefits of combined formation and ground-effect flight stems from two main observations, both discussed earlier: (1) a larger-span wing achieves the same ground-effect benefit (same σ) as a smaller-span wing but at a larger height above ground, h , and (2) a formation at near-optimal lateral separation behaves like an effectively large-span wing with respect to induced drag. Based on these two observations, a hypothesis was made that a formation of several wings will be able to experience ground-effect benefits at larger heights than a single wing. Owing to the fact that safety issues and the demand for very precise control of h become increasingly important for flight in close proximity to the ground, it is worthwhile exploring concepts that will enable the achievement of ground-effect benefits at large values of h . With this goal, combined formation and ground-effect flight was studied and the results are presented in this subsection.

As a first step in examining the combined effect of formation and ground-

effect flight, the current method was used to determine the optimum downwash and optimum lift distributions for three planar wings flying in formation at various h . A lateral separation of $Y/b = 1.02$, along with a zero vertical separation, were used for this part of the study.

Figure 3.11(a) shows the resulting nondimensional Trefftz-plane downwash distributions. The $h/b = 0.02$ case is intended to represent an extreme ground-effect configuration. The linear variation of downwash across the span of each wing is clearly seen. Figure 3.11(b) shows the corresponding spanwise lift distributions on the wings. With trends similar to those observed for the single wing in ground effect, the downwash magnitude decreases with decreasing height above ground (Fig. 3.11(a)). The load distribution that is most parabolic in shape in Fig. 3.11(b) corresponds to the smallest height, $h/b = 0.02$. It is interesting to note that for this lateral separation, the spanwise downwash and lift distributions for $h/b = 0.02$ are very close to those observed for the single planar wing in ground effect shown earlier in Fig. 3.9(a) and 3.9(b).

Although the optimal loading is noticeably different from an elliptical loading, especially for close formations and small ground clearances (Fig. 3.11(b), $h/b = 0.02$), the drag ratios (not shown) for elliptically-loaded wings in formations are nearly the same as those for the corresponding optimally-loaded wing formations. For this reason, only the elliptically-loaded cases are presented in the remainder of this study.

As a second step in the study of combined formation and ground-effect flight, the variations of the induced-drag ratio, σ , for formations of three and 25 wings as a function of lateral separation Y/b were examined for flight both in and out of ground effect. In all cases, the vertical separation between the wings was zero. The 25-wing case was selected as an example of a very large formation similar to a flock of birds in flight. For both formations, each wing was elliptically loaded

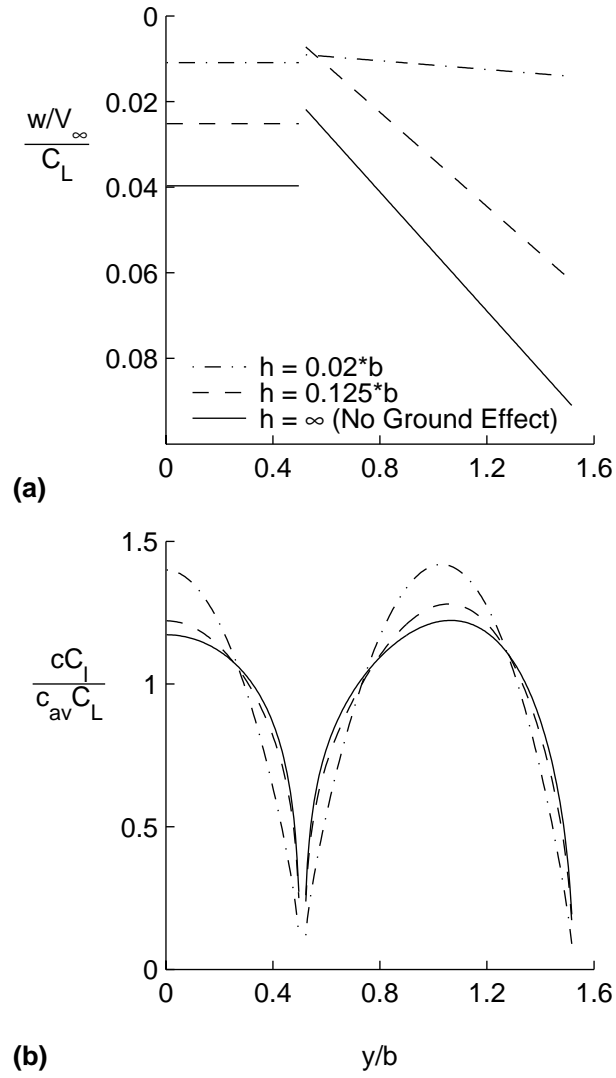


Figure 3.11: Wing formation in ground effect: (a) optimum Trefftz-plane downwash distributions and (b) optimum spanload distributions at various h .

and the lateral separation was increased from $Y/b = 0$ to 2.5. For the case of flight IGE, each formation was examined at a representative height of $h/b = 0.5$.

For the three-wing formation in Fig. 3.12(a), it can be seen that the optimum lateral separation for the formation both IGE and OGE is at $Y/b = 0.9$. At any Y/b , the σ for the IGE case of this formation is less than that for the OGE case by approximately 0.08 over the range of Y/b plotted in Fig. 3.12(a). For the larger formation of 25 wings seen in Fig. 3.12(b), the optimum lateral separation is nearly the same as for the three-wing formation, at $Y/b = 0.89$. At this optimum lateral separation, the σ is 0.19, implying that the drag reduction is 81% compared to 25 wings flying in isolation out of ground effect. For both formations, it can be stated that ground effect does not influence the optimum lateral separation for the induced drag ratio. Unlike the three-wing formation, the difference in the drag ratio between the OGE and IGE cases of the 25-wing formation varies considerably with lateral separation. In particular, there is little difference in σ between the OGE and IGE cases for Y/b between 1.05 and 1.25 where adjacent wings tips are closely spaced but do not overlap. When the wingtips overlap, the difference in the σ between OGE and IGE cases increases with decreasing Y/b .

It is interesting to note that for the 25-wing formation, there are distinct multiple local minima, with the prominent second and third local minima located at $Y/b = 0.47$ and $Y/b = 0.32$. These lateral-separation values are approximately one-half and one-third of the lateral separation of $Y/b = 0.89$ for the first minimum. These multiple local minima also occur for the IGE case at the same Y/b values. A study of the relative contributions of the different f terms in Eq. 3.24 can be used to explain the occurrence of these multiple local minima. The primary minimum at $Y/b = 0.89$ occurs because of strong favorable interference between every wing and its adjacent neighbor (wings i and $i + 1$). The second local minimum at $Y/b = 0.47$ occurs because of strong favorable interference between pairs

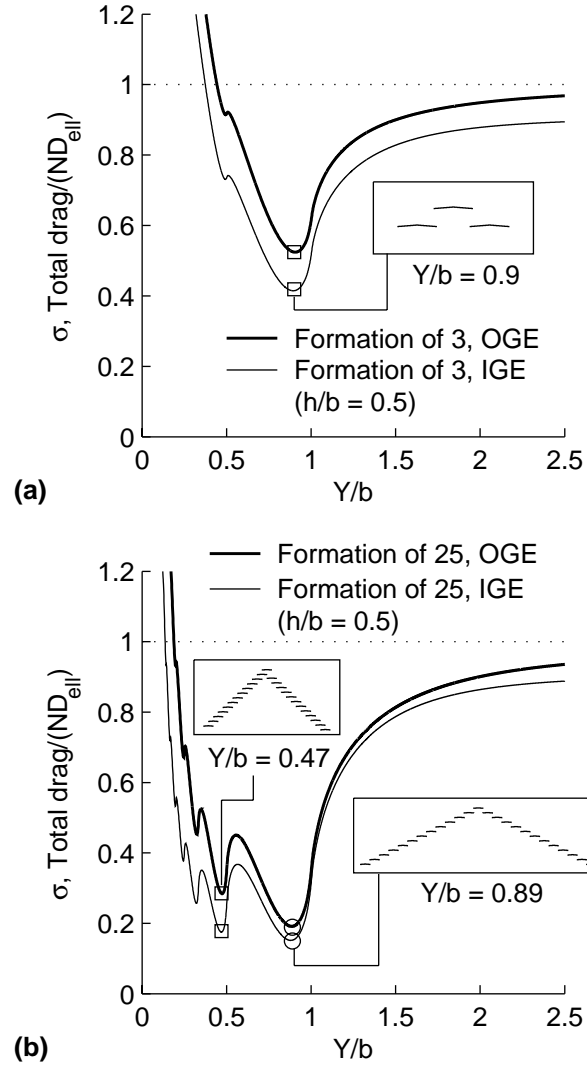


Figure 3.12: Exact results for the effect of lateral separation on drag ratio for three- and 25-wing formations in and out of ground effect with insets showing the plan views of formation geometries at arbitrary streamwise spacings.

formed by a wing and its next-to-immediate neighbor (wings i and $i+2$). Likewise, the third local minimum occurs because of strong favorable interference between wings i and $i+3$.

Additionally, from a study of the relative contributions of the different g terms in Eq. 3.25, it can be seen that there is stronger favorable interference between pairs formed by a wing and the image of its adjacent neighbor for $Y/b = 0.47$ than for $Y/b = 0.9$. As a result, the σ values for the first and second minima in the IGE case differ by only 0.025. In other words, the drag difference between the two minima in the IGE case is only 2.5% of $25 D_{ell}$. With increasing number of wings, the second minimum for the IGE case becomes even more pronounced. For example, for a 100-wing formation at $h/b = 0.5$, the second minimum has slightly less drag than the primary minimum. Although the drag ratio at the second minimum is close to that at the first minimum, the drag in the vicinity of this second minimum is more sensitive to the lateral separation, whereas the first minimum at $Y/b = 0.89$ is comparatively more flat. The formation plan views shown in the insets in Fig. 3.12(b) illustrate the differences in the lateral separation at the primary and secondary minima, and have been shown with an arbitrary streamwise spacing between the wings. The right leg of the vee-shape for $Y/b = 0.47$ has been displaced slightly downstream of the left leg to avoid collision between the two wings on either side of the lead.

Although, for $Y/b < 1$ the drag-ratio variation for the 25-wing formation has considerable waviness, it is worth noting that there is a wide range of Y/b from approximately 0.3 to 1.05 that results in at least 50% drag reduction compared to 25 wings flying solo and OGE. This large range of beneficial lateral separations and the multiple local minima for large formations may partly explain the considerable imprecision and variation in lateral separation that is observed in birds flying in formation.¹⁶ For very small lateral separations in the OGE case, there is a steep

increase with the drag ratio reaching a value of 25 for $Y/b = 0$, a value that matches the exact result from Munk's stagger theorem. More generally, it can be shown that the σ for N wings flying OGE at $Y/b = 0$ and $Z/b = 0$ is exactly N .

As a third step in the examination of combined formation and ground-effect flight, the effect of height above ground was studied for a single wing and for wing formations. Figure 3.13 presents the drag ratio for a single wing and for formations of three and 25 wings in ground effect at various heights above ground. For both formations, the results have been plotted for two lateral-separation values of $Y/b = 0.9$, corresponding to the optimum lateral separation, and $Y/b = 1.1$, corresponding to a separation with no lateral overlap of wing tips. These two values have been used to further illustrate the important effects of wing tip overlap on drag benefits. The drag ratio of each formation OGE has also been plotted, which corresponds to the asymptote as $h/b \rightarrow \infty$. For any given formation, the difference between the OGE drag ratio and the IGE drag ratio, for a certain h/b , is a measure of the ground-effect benefit for that h/b .

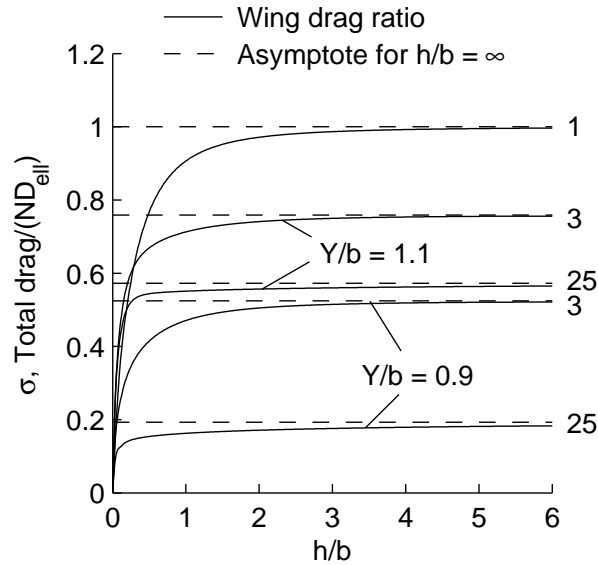


Figure 3.13: Drag ratios for a single wing and for formations of three and 25 wings in ground effect.

The drag-ratio variation for the single-wing case is the same as that shown earlier in Fig. 3.8 and serves as a good reference. It is seen that for small ground clearances of $h/b < 1$, the reduction in σ due to ground effect is significant for the single wing and for the three-wing formations. However, the reduction in σ at these clearances is comparatively marginal for the 25-wing formations. At these small ground clearances, the images of neighboring wings are in regions of adverse interference. As a result, the cumulative contribution of the g -terms in Eq. 3.25 is adverse for large formations and this adverse contribution detracts from the favorable effects between each wing and its own image. For large ground clearances of $h/b > 2$, the situation is reversed: large formations experience greater reductions in σ when compared to a single wing or smaller formations. At large ground clearances, the favorable effects between each wing and its own image diminish rapidly with increasing h/b , as seen from the results of the single-wing case. However, for large formations, the cumulative effect of the images of adjacent wings become favorable because the images of neighboring wings are in regions of favorable interference. Although this effect is small, it persists even at relatively large ground clearances of $h/b \approx 4$. As a result, there is a small, but noticeable, reduction in σ for large formations even at large ground clearances, as seen for the 25-wing formations in Fig. 3.13. Thus, combined formation and ground-effect flight results in a small additional reduction in induced drag, even at large ground clearances, and may at least partly explain why some species of migrating birds are seen to fly in formation close to the ground.

The importance of maintaining the optimal lateral separation of approximately $Y = 0.9b$ is seen by comparing the two drag-ratio curves for the 25-wing formations in Fig. 3.13. For any given h/b , the formation induced drag for $Y = 1.1b$ is almost three times that obtained with the optimum separation of $Y = 0.9b$. Thus, it is important to maintain a small lateral overlap of wing tips for large formations,

whether OGE or IGE. As seen from the results of 3.12(b), it is better to err on the smaller- Y/b side of the optimum lateral separation than on the larger- Y/b side. That is, a wide range of Y/b values that result in lateral wing-tip overlap provide greater drag reduction than non-overlapped wings with $Y/b > 1.1$. It is to be noted that lateral overlap of wings does not imply that the aircraft have to fly close to each other. As pointed out by Munk's stagger theorem, the total formation induced drag is independent of the streamwise separation between the wings as long as the spanwise lift distributions are maintained. Thus, the aircraft can be well separated in the streamwise direction for safety.

3.3.3 Optimal Vee-Formation Shapes

Migrating birds are often seen flying in vee-shaped formations. Of particular interest in the current study was the difference in the shape of the optimal vee formation for OGE and IGE flight. The optimum vee-formation shape was found by setting the requirement that each wing have equal induced drag. Fig. 3.14(a) shows the resulting optimum formations for a formation of 25 wings IGE and OGE. A lateral separation of $Y/b = 0.9$ with zero vertical separation was used. A clearance of $h/b = 1.0$ was used for ground-effect flight. It can be seen that the optimal shape of the vee formation is not an exact "V", but a shape that is more swept at the tips and rounded at the apex. Similar optimal vee-formation shapes were reported by Lissaman and Shollenberger¹⁰ and by Hummel.¹² The differences in formation shape in and out of ground effect are insignificant, indicating that the optimum vee shape for the formation OGE would serve just as well for the formation IGE. The results in Fig. 3.14(a) show that, for equipartition of drag, the wings near the apex of the vee are very closely spaced. Such close separation may not be practical for routine aircraft flight operations. Thus, it may be necessary to compromise on the equipartition of drag in order to decrease the risk of collision.

Additionally, it must be noted that the exact shape of this vee formation may not be correct for bird formations, where the flapping frequency of the wings may have an additional effect on longitudinal separation.

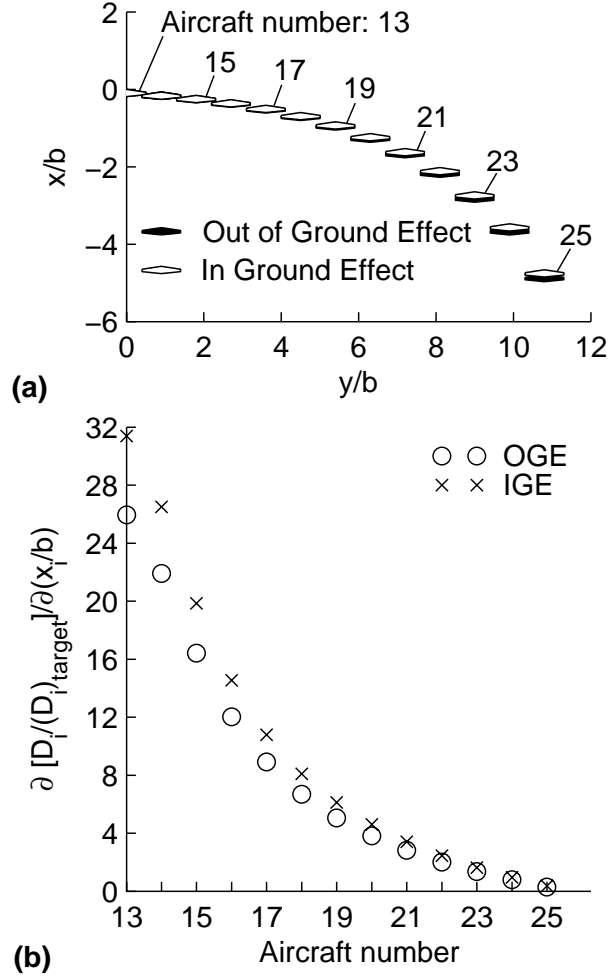


Figure 3.14: A 25-wing formation in and out of ground effect ($h/b = 1.0$): (a) optimum vee-formation shape, and (b) gradient of individual induced drag with streamwise location.

It was of interest to determine the natural stability of the streamwise position of each individual in the formation, to see if the vee formation is a natural and stable flight mode. This stability was determined by examining the variation of the individual induced drag with streamwise location. Figure 3.14(b) is a plot of the gradient of individual induced drag (nondimensionalized by the target

individual induced drag for the optimum vee formation) with respect to streamwise location for each wing on the right-hand side of the vee formation. The wings are numbered from 13 to 25, with wing 13 denoting the one at the apex of the vee formation and wing 25 denoting that at the right tip of the formation. Lissaman and Shollenberger¹⁰ observed that if a bird moves ahead of the vee formation, more power is required for it to maintain the same airspeed, and when flying aft of the vee formation less power is required. In either case, the bird will tend to return to its original position within the vee formation. This result is confirmed in the current work by the fact that the gradients in Fig. 3.14(b) are positive for all wings, with positive x pointing in the direction of flight. The differences in gradients between the OGE and IGE cases are small, indicating that ground effect does not significantly affect the position stability.

For an aircraft flying at the tips of the formation, however, changes in streamwise location do not result in significant changes in induced drag, as seen in Fig. 3.14(b). With gradients approaching zero, the aircraft located at the tip of the formation will find it more difficult to maintain position in formation. Weimerskirch and colleagues¹⁵ witnessed this behavior during the experiments conducted on a formation of great white pelicans and state that pelicans often had difficulty staying within formation when flying at the tips.

3.4 Summary

The objective of the current study was to examine the benefits of formation flight both in and out of ground effect, as a potentially effective approach for drag reduction of future aircraft. The wings analyzed in the study were loaded ideally in one of two ways: with an optimum lift distribution or with an elliptical lift distribution. For determining optimum lift distributions, an optimum-downwash-

based approach using a vortex-lattice implementation was used. For the cases with elliptically-loaded planar wings, an exact approach was developed, which is based on the interference-drag between wings in a formation. Whereas the optimum-loading approach is not applicable for wing formations with overlapping wake traces, the exact approach developed for elliptically-loaded planar wings allowed one to examine the effects of lateral overlap of wings on the formation induced drag.

A comparison of optimally-loaded and elliptically-loaded planar wings showed that, for any formation in or out of ground effect, the two loading scenarios have virtually the same drag. In the analysis of lateral separation between wings, it was observed that for a formation of wings at any ground clearance, the optimum lateral separation between adjacent wings corresponds to a lateral overlap of approximately 9% of the wing span. For large formations, multiple local minima were observed in the drag variation with lateral separation, due to variations in the interference drag between each wing and its successive neighbors. For the large formation in ground effect, little change was observed in the lateral separations corresponding to the local minima, thus resulting in nearly the same drag.

When examining combined formation and ground-effect flight, it was seen that large formations are able to achieve a small, but noticeable benefit due to ground effect even at a relatively large ground height of four wing spans. When adjusting the streamwise placement of the wings within the formation for an equal distribution of individual induced drag, a vee-formation results. This vee-formation shape was found to be practically independent of the ground clearance, and provides an automatic streamwise-position stability for the wings. This stability was found to be the highest for the lead wing, which then degrades toward the tips of the vee formation.

Chapter 4

Concluding Remarks

The focus of this dissertation was to explore two different approaches for the reduction of aircraft drag: (1) multiple spanwise trailing-edge flaps and (2) formation and ground-effect flight. Each approach has the potential for significant drag savings if applied, and each approach was motivated by bird flight studies—a long-time source of inspiration for many aerodynamicists. To improve the performance and efficiency of today’s aircraft is a never-ending endeavor, and with advances in precision measurement, aircraft control, and adaptive wing technology, such innovative approaches, as those examined in this dissertation, are becoming more feasible alternatives for drag reduction. Therefore, the main goal of this dissertation was to assess the drag benefits of the two selected approaches. It is believed that the research presented here will further increase interest in such flight techniques, and thus advance their progression toward becoming viable solutions for drag reduction of future aircraft.

The first part of this research presents a study in the use of multiple spanwise trailing-edge flaps for reducing both induced and profile drag. With increasing interest in the use of variable spanwise camber and the future automation of an adaptive wing, the primary focus of the study was to provide an approach that determines optimum flap angles that produce an ideal lift distribution for a particular adaptation objective: minimization of drag, or minimization of drag

with a constraint on the wing root-bending moment. The approach developed in this research uses the concept of additional and basic lift distributions, as well as the understanding of the aerodynamics that bring about a minimum in profile and induced drag. Flap-angle distributions for different flight conditions were determined for two examples: (1) a planar wing, and (2) a nonplanar wing. The numerical approach was found to be effective in determining the optimum flap angles that result in a minimization of both induced and profile drag, for a wide range of lift coefficients. In conducting aircraft performance simulations using the optimum flap schedules, an increase in maximum velocity, maximum range, and maximum endurance were observed when compared to the zero-flap setting case. The approach was also found to be successful in determining flap angles that would relieve the wing root-bending moment when applying a root-bending moment constraint.

Overall, the approach developed for the case study of multiple trailing-edge flaps is effective in determining flap angles for the reduction of drag, with or without a wing root-bending moment constraint. The resulting improvement in aircraft performance using the determined optimum flap-angles schedules demonstrates the benefits of using variable spanwise camber, and further promotes its use for aircraft drag reduction. The idea of an automated adaptive wing is not too far in the future, and it is believed that the research presented here makes a strong case for further development of such a system to be used on future aircraft.

The second part of this dissertation examined the use of formation and ground-effect flight for aircraft drag reduction, and in particular, the benefits of combined formation and ground-effect flight. In this study, the theoretical models used assume rigid, inviscid wakes that trail without rollup in the downstream direction. The wings were loaded ideally in one of two ways: with an optimum lift distribution, or with a prescribed elliptical lift distribution. To determine the optimum lift

distributions, an optimum-downwash-based approach using vortex lattice implementation was used. When comparing the total induced drag of optimally-loaded and elliptically-loaded planar wing formations, both in and out of ground effect, it was observed that the two loading scenarios had virtually the same drag. The benefit of using elliptical loading is that the target loading for each wing is independent of the formation geometry or height above ground. However, in order to generate the target lift distribution, there is a need for an appropriate twist or camber variation across the span of each wing. Because this spanwise geometry variation is dependent on the formation configuration and ground clearance, the wing geometry will need to adapt its shape, perhaps through the use of multiple trailing-edge flaps.

The effect of lateral separation between wings on formation induced drag was also examined. As the optimum-loading method is not valid for formations in which the wake traces for the wings overlap, an exact approach was developed for elliptically-loaded planar wings which allows examination of formation configurations with overlapping wake traces. The exact approach was developed using the exact interference-drag solution of a two-wing formation, which was extended to a formation of several wings. For any formation of planar wings at any ground clearance, the optimum lateral separation between adjacent wings corresponds to a lateral overlap of approximately 9% of the wing span. At this optimum lateral separation, the favorable interference between adjacent wings is maximized. This optimum lateral separation is close to that observed in wind-tunnel and flight experiments. For large formations, multiple local minima were observed in the drag variation with lateral spacing. These multiple local minima were shown to occur because of the variations in interference drag between each wing and its successive neighbors. For large formations in ground effect, it was shown that the lateral separations corresponding to the primary and secondary local minima resulted in

nearly the same drag. The presence of these local minima with nearly the same drag may explain the considerable variations and imprecision in lateral separation that are often observed in bird formations.

The results for combined formation and ground-effect flight show that large formations are able to achieve a small, but noticeable, benefit due to ground effect even at a relatively large ground height of four wing spans. When the streamwise separation is adjusted for equal distribution of the drag benefit among all the wings in a formation, a vee-shaped formation results. This vee-formation shape is practically independent of the ground clearance. When flying in such a vee formation, the sensitivity of the individual-aircraft drag due to changes to the streamwise position provides automatic streamwise-position stability for the aircraft. This stability is highest for the lead aircraft and degrades toward the tips of the vee formation. This result supports observations made by other researchers that pelicans located at the tips of a vee-shaped formation often have difficulty maintaining their position.

With the potential for achieving dramatic improvements in aircraft performance, formation and ground-effect flight techniques hold significant promise for use in future aeronautical systems. Although the realization of their everyday use is still far in the future, it is believed that this research provides valuable insight into the aerodynamics of formation and ground-effect flight by a quantification of the benefits for ideally-loaded wings in configurations that maximize the favorable interference between the wings.

Chapter 5

Future Work

This research was undertaken with the objective of assessing the drag benefits of using multiple trailing-edge flaps and formation and ground-effect flight. As presented in this dissertation, each approach has potential for significant drag savings in their application to aircraft. Suggested future work combines the theory of both approaches, in examining optimum flap angles for minimum induced drag on multiple lifting surfaces.

As presented in Chapter 3, it was determined that an elliptically-loaded wing formation has minimum induced drag when there is a 9%-span lateral overlap of wingtips. It was also shown that when comparing the total induced drag of optimally-loaded and elliptically-loaded planar wing formations, both in and out of ground effect, the two loading scenarios had virtually the same drag. The benefit of using elliptical loading is that the target loading for each wing is independent of the formation geometry or height above ground. However, in order to generate the target lift distribution, there is a need for an appropriate twist or camber variation across the span of each wing. Because this spanwise geometry variation is dependent on the formation configuration and ground clearance, the wing geometry will need to adapt its shape. Multiple trailing-edge flaps can be used for wing adaptation, as shown in Chapter 2, and it is of interest to determine optimum flap angles to maintain an elliptical loading on each wing in the

formation, both in and out of ground effect, at a desired lateral separation.

The concept of multiple trailing-edge flaps on multiple lifting surfaces can also be extended to a tandem-wing configuration. In a tandem-wing configuration, the aircraft is equipped with a canard that is of a span close to the span of the aft wing. With the use of multiple trailing-edge flaps on both the canard and the wing, the wing loading can be redistributed to achieve minimum induced drag. However, there is an additional consideration that must be met, in that the canard is also usually used for pitch control. Therefore, the optimum flap angles for minimum induced drag must also effectively trim the aircraft. The placement of the canard in relation to the wing also has an important influence on the resulting aircraft drag and the trim and control effectiveness of the canard. So special attention must be placed on the horizontal and vertical separation between the wing and the canard.

For determining optimum flap-angle distributions for multiple lifting surfaces, the numerical approach presented in Chapter 2 must be extended to handle a system of wings versus one wing. Additional modifications to the approach must also provide a means to ensure trim requirements are met, specifically for the tandem-wing configuration. It is believed that successful determination of optimum flap angles for multiple wings will further demonstrate the effectiveness of the drag reduction approaches presented in this dissertation, as well as the additional benefits that can be gained from the use of trailing-edge flaps.

Chapter 6

References

- ¹ Stillson, B., *Wings: Insects, Birds, Men*, The Bobbs-Merrill Company, Inc., New York, 1954.
- ² Bolonkin, A. and Gilyard, G. B., “Estimated Benefits of Variable-Geometry Wing Camber Control for Transport Aircraft,” NASA TM 1999-206586, October 1999.
- ³ Thornton, S. V., “Reduction of Structural Loads using Maneuver Load Control in the Advanced Fighter Technology Integration (AFTI)/F-111 Mission Adaptive Wing,” NASA TM 4526, September 1993.
- ⁴ Stanewsky, E., “Aerodynamic benefits of adaptive wing technology,” *Aerospace Science and Technology*, Vol. 4, No. 7, 2000, pp. 439–452.
- ⁵ Monner, H. P., Breitbach, E., Bein, T., and Hanselka, H., “Design aspects of the adaptive wing — the elastic trailing edge and the local spoiler bump,” *The Aeronautical Journal*, Vol. 104, February 2000, pp. 89–95.
- ⁶ Spillman, J. J., “The use of variable camber to reduce drag, weight and costs of transport aircraft,” *Aeronautical Journal*, January 1992, pp. 1–9.
- ⁷ McAvoy, C. W. and Gopalarathnam, A., “Automated Trailing-Edge Flap for

Airfoil Drag Reduction Over a Large Lift-Coefficient Range,” AIAA Paper 2002-2927, June 2002.

- ⁸ Gopalarathnam, A. and McAvoy, C. W., “Automated Cruise Flap for Airfoil Drag Reduction Over a Large Lift Range,” *Journal of Aircraft*, Vol. 39, No. 6, November–December 2002, pp. 981–988.
- ⁹ Wieselsberger, C., “Beitrag zur Erklarung des Winkelfluges einiger Zugvogel,” *Zeitschrift fur Flugtechnik und Motorluftschiffahrt*, Vol. 5, 1914, pp. 225–229.
- ¹⁰ Lissaman, P. B. S. and Shollenberger, C. A., “Formation Flight of Birds,” *Science*, Vol. 168, No. 3934, May 1970, pp. 1003–1005.
- ¹¹ Hummel, D., “Aerodynamic Aspects of Formation Flight in Birds,” *Journal of Theoretical Biology*, Vol. 104, No. 3, 1983, pp. 321–347.
- ¹² Hummel, D., “Formation Flight as an Energy-Saving Mechanism,” *Israel Journal of Zoology*, Vol. 41, No. 3, 1995, pp. 261–278.
- ¹³ Hummel, D., “The Use of Aircraft Wakes to Achieve Power Reductions in Formation Flight,” AGARD CP-584, May 1996.
- ¹⁴ Hainsworth, F. R., “Precision and Dynamics of Positioning by Canada Geese Flying in Formation,” *Journal of Experimental Biology*, Vol. 128, No. 1, 1987, pp. 445–462.
- ¹⁵ Weimerskirch, H., Martin, J., Clerquin, Y., Alexandre, P., and Jiraskova, S., “Energy Saving in Flight Formation,” *Nature*, Vol. 413, No. 6857, October 2001, pp. 697–698.
- ¹⁶ Hainsworth, F. R., “Induced Drag Savings from Ground Effect and Formation Flight in Brown Pelicans,” *Journal of Experimental Biology*, Vol. 135, No. 1, 1988, pp. 431–444.

- ¹⁷ Wieselsberger, C., “Über den Flugwiderstand in der Nahe des Boden,” *Zeitschrift für Flugtechnik und Motorluftschiffahrt*, Vol. 10, 1914, pp. 145.
- ¹⁸ de Haller, P., “La Portance et la Trainee Induite Minimum d’une Aile au Voisinage du Sol,” *Mitteilungen aus dem Institut für Aerodynamik der Technische Hochschule, Zurich* 5, 1936.
- ¹⁹ Ashill, P. R., “On the Minimum Induced Drag of Ground Effect Wings,” *Aeronautical Quarterly*, Vol. XXI, August 1970, pp. 211–232.
- ²⁰ Rozhdestvensky, K. V., *Aerodynamics of a Lifting System in Extreme Ground Effect*, Springer, New York, 2000.
- ²¹ Katz, J. and Plotkin, A., *Low-Speed Aerodynamics*, Cambridge Aerospace Series, Cambridge University Press, Cambridge, UK, 2001.
- ²² Reid, E. G., “A Full-Scale Investigation of Ground Effect,” NACA Rep. 265, 1928.
- ²³ Curry, R. E. and Bowers, A. H., “Ground-Effect Analysis of a Jet Transport Airplane,” NASA TM 85920, January 1985.
- ²⁴ Curry, R. E., Moulton, B. J., and Kresse, J., “An In-Flight Investigation of Ground Effect on a Forward-Swept Wing Airplane,” NASA TM 101708, September 1989.
- ²⁵ Rayner, J. M. V., “On the aerodynamics of animal flight in ground effect,” *Phil. Trans. R. Soc. Lond. B*, Vol. 334, No. 1269, 1991, pp. 119–128.
- ²⁶ Feifel, W. M., “Optimization and Design of Three-Dimensional Aerodynamic Configurations of Arbitrary Shape by a Vortex Lattice Method,” NASA SP 405, May 1976, pp. 71–88.

- ²⁷ Beukenberg, M. and Hummel, D., “Aerodynamics, Performance and Control of Airplanes in Formation Flight,” ICAS 90-5.9.3, September 1990.
- ²⁸ Iglesias, S. and Mason, W. H., “Optimum Spanloads in Formation Flight,” AIAA Paper 2002-0258, January 2002.
- ²⁹ Frazier, J. W. and Gopalathnam, A., “Optimum Downwash Behind Wings in Formation Flight,” *Journal of Aircraft*, Vol. 40, No. 4, July–August 2003, pp. 799–803.
- ³⁰ Gingras, D. R., Player, J. L., and Blake, W. B., “Static and Dynamic Wind Tunnel Testing of Air Vehicles in Close Proximity,” AIAA Paper 2001-4137, August 2001.
- ³¹ Blake, W. B. and Gingras, D. R., “Comparison of Predicted and Measured Formation Flight Interference Effects,” *Journal of Aircraft*, Vol. 41, No. 2, 2004, pp. 201–207.
- ³² Wagner, G., Jacques, D., Blake, W., and Pachter, M., “Flight Test Results of Close Formation Flight for Fuel Savings,” AIAA Paper 2002-4490, August 2002.
- ³³ Vachon, M. J., Ray, R. J., Walsh, K. R., and Ennix, K., “F/A-18 Aircraft Performance Benefits Measured During The Autonomous Formation Flight Project,” AIAA Paper 2002-4491, August 2002.
- ³⁴ Ray, R. J., Cobleigh, B. R., Vachon, M. J., and John, C. S., “Flight Test Techniques Used to Evaluate Performance Benefits During Formation Flight,” AIAA Paper 2002-4492, August 2002.
- ³⁵ Laurenzo, R., “A Long Wait for Big Wigs,” *Aerospace America*, Vol. 41, No. 6, June 2003, pp. 36–40.

- ³⁶ Kroo, I., “Innovations in Aeronautics,” AIAA Paper 2004-0001, January 2004.
- ³⁷ McMasters, J. H. and McLean, J. D., “The Formation Flight of Human Powered Aircraft Across the English Channel in the Spring,” *Swiss Aero Revue*, December 1979, [XVIth Congress of the Organization Scientifique et Technique International du Vol-a-Voilé [OSTIV], Château roux, France, 1978.].
- ³⁸ Lissaman, P., “Simplified Analytical Methods for Formation Flight and Ground Effect,” AIAA Paper 2005-851, January 2005.
- ³⁹ Marino, L., “Induced-drag reduction of wing-wings and wings-ground configurations,” *Aeronautical Journal*, October 2004, pp. 523–530.
- ⁴⁰ Kroo, I. M., “A General Approach to Multiple Lifting Surface Design and Analysis,” AIAA Paper 84–2507, October 1984.
- ⁴¹ Grasmeyer, J., “A Discrete Vortex Method for Calculating the Minimum Induced Drag and Optimum Load Distribution for Aircraft Configuration with Noncoplanar Surfaces,” Vpi-aoe-242, January 1997.
- ⁴² Grosser, M., *Gossamer Odyssey*, Houghton Mifflin Company, Boston, 1981.
- ⁴³ Burke, J. D., “The Gossamer Condor and Albatross: A Case Study in Aircraft Design,” AeroVironment Inc. Report No. AV-R-80/540, June 1980.
- ⁴⁴ King, R. M. and Gopalarathnam, A., “Ideal Aerodynamics of Ground-Effect and Formation Flight,” AIAA Paper 2004-0906, January 2004.
- ⁴⁵ King, R. M. and Gopalarathnam, A., “Ideal Aerodynamics of Ground-Effect and Formation Flight,” *Journal of Aircraft*, Accepted for publication, in press.
- ⁴⁶ Kroo, I., “Drag due to Lift: Concepts for Prediction and Reduction,” *Annual Review of Fluid Mechanics*, Vol. 33, 2001, pp. 587–617.

- ⁴⁷ Iannotta, B., “Vortex Draws Flight Research Forward,” *Aerospace America*, Vol. 40, No. 3, March 2002, pp. 26–30.
- ⁴⁸ Jones, R. T., “The Spanwise Distribution of Lift For Minimum Induced Drag of Wings Having a Given Lift and a Given Bending Moment,” NACA TN 2249, December 1950.
- ⁴⁹ Munk, M. M., “The Minimum Induced Drag of Aerofoils,” NACA Rep. 121, 1921.
- ⁵⁰ Blackwell, J. A., Jr., “Numerical Method to Calculate the Induced Drag or Optimum Loading for Arbitrary Non-Planar Aircraft,” NASA SP 405, May 1976, pp. 49–70.
- ⁵¹ Pfenninger, W., “Investigation on Reductions of Friction on Wings, in Particular by Means of Boundary Layer Suction,” NACA TM 1181, August 1947.
- ⁵² Pfenninger, W., “Experiments on a Laminar Suction Airfoil of 17 Per Cent Thickness,” *Journal of the Aeronautical Sciences*, April 1949, pp. 227–236.
- ⁵³ Somers, D. M., “Design and Experimental Results for a Flapped Natural-Laminar-Flow Airfoil for General Aviation Applications,” NASA TP 1865, June 1981.
- ⁵⁴ Viken, J. K., *Aerodynamic Design Considerations and Theoretical Results for a High Reynolds Number Natural Laminar Airfoil*, Master’s thesis, George Washington University, 1983.
- ⁵⁵ McGhee, R. J., Viken, J. K., Pfenninger, W., Beasley, W. D., and Harvey, W. D., “Experimental Results for a Flapped Natural-Laminar-Flow Airfoil with High Lift/Drag Ratio,” NASA TM 85788, May 1984.

- ⁵⁶ Viken, J. K., “Boundary-Layer Stability and Airfoil Design,” *Laminar Flow Aircraft Certification*, NASA CP 2413, 1985, pp. 1–30.
- ⁵⁷ Althaus, D. and Wortmann, F. X., *Stuttgarter Profilkatalog I*, Friedr. Vieweg & Sohn, Braunschweig, 1981.
- ⁵⁸ Drela, M., “Elements of Airfoil Design Methodology,” *Applied Computational Aerodynamics*, edited by P. A. Henne, Vol. 125, AIAA, Washington, DC, 1990, pp. 167–189.
- ⁵⁹ Althaus, D., *Niedrig-geschwindigkeits-profile*, Friedr. Vieweg & Sohn Verlagsgesellschaft mbH, Braunschweig/Wiesbaden, 1996.
- ⁶⁰ Anderson, R. F., “Determination of the Characteristics of Tapered Wings,” NACA Rept. 572, 1936.
- ⁶¹ Abbott, I. H. and von Doenhoff, A. E., *Theory of Wing Sections*, McGraw-Hill Book Company, 1949.
- ⁶² Kuethe, A. M. and Chow, C.-Y., *Foundations of Aerodynamics: Bases of Aerodynamic Design*, John Wiley & Sons, Inc., 1986.
- ⁶³ Jepson, J. and Gopalathnam, A., “Inverse Design of Adaptive Airfoils with Aircraft Performance Considerations,” AIAA Paper 2004-0028, January 2004, accepted for publication in *Journal of Aircraft*.
- ⁶⁴ Drela, M., “XFOIL: An Analysis and Design System for Low Reynolds Number Airfoils,” *Low Reynolds Number Aerodynamics*, edited by T. J. Mueller, Vol. 54 of *Lecture Notes in Engineering*, Springer-Verlag, New York, June 1989, pp. 1–12.

- ⁶⁵ Gopalarathnam, A. and McAvoy, C. W., “Effect of Airfoil Characteristics on Aircraft Performance,” *Journal of Aircraft*, Vol. 39, No. 3, May–June 2002, pp. 427–433.
- ⁶⁶ Glauert, H., *The Elements of Aerofoil and Airscrew Theory*, Cambridge University Press, Cambridge, 1930.
- ⁶⁷ von Kármán Th. and Burgers, J. M., *General Aerodynamic Theory—Perfect Fluids*, Vol. 2 of *Aerodynamic Theory*, Julius Springer, 1935.
- ⁶⁸ Prandtl, L., “Induced Drag of Multiplanes,” NACA TN 182, March 1924.
- ⁶⁹ The MathWorks, Inc., *Symbolic Math Toolbox for Matlab: User’s Guide*, 2004.

Appendix A

Modeling of Lateral Symmetry and Ground Reflections

This appendix presents a brief description of how the symmetry of a formation of wings, in or out of ground effect, can be implemented into the vortex-lattice method to significantly reduce the computational time. Based on the standard techniques presented in Ref. 21, when symmetry exists between the left and right halves of a wing formation, or even about the ground plane when modeling a formation in ground effect, a rather simple method can be used to include these features in the numerical scheme. This modification to the vortex-lattice method only affects the computation of the influence coefficient matrix \mathbf{I} , which is used to relate the Γ distributions on the wings and the associated Trefftz-plane downwash distributions, w , as presented in Eq. A.1.

$$\mathbf{I} \cdot \Gamma = \mathbf{w} \tag{A.1}$$

When symmetry is not taken into consideration, the influence coefficient matrix \mathbf{I} is a square $n \times n$ matrix, where n is the number of horseshoe vortices used to approximate the bound vorticity distribution on all of the wings and the trailing vorticity shed behind them. In this matrix, the (i, j) element represents the induced downwash at control point i due to the velocity induced by horseshoe

vortex j . However, if a lateral symmetry of the formation of wings exists, the influence coefficient matrix can be reduced in size by one quarter.

For example, consider the simple case of a single symmetric wing, as seen in Fig. A.1, where the vorticity distribution is approximated using four horseshoe vortices.

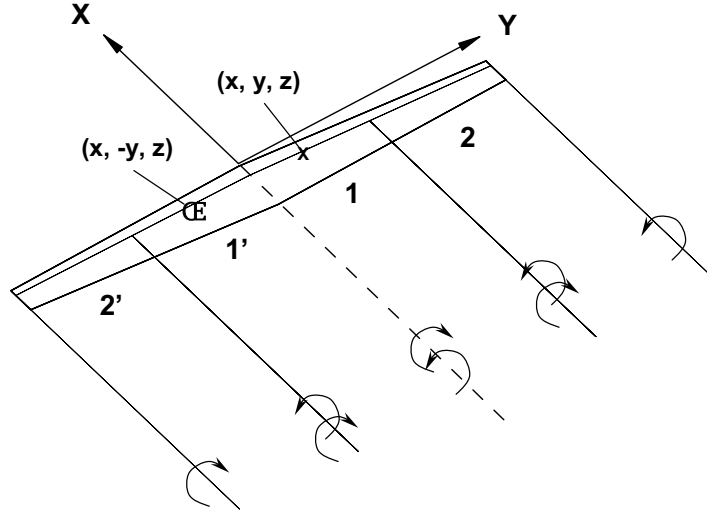


Figure A.1: Single wing with lateral symmetry, with vorticity distribution modeled with four horseshoe vortices.

Now, consider the determination of the induced downwash at control point 1, located at (x, y, z) , due to the velocity induced by horseshoe vortex 2. Each horseshoe vortex has a constant value for the bound vortex strength Γ . Due to the lateral symmetry, the image horseshoe vortex 2' has the same strength as horseshoe vortex 2, and its effect can be evaluated by determining the influence of the actual vortex at point $(x, -y, z)$. By simply reflecting the control point into the left-plane of symmetry, the influence of two horseshoe vortices on a single control point can be accurately computed. Therefore, only the vortices of the right-half the wing needs to be modeled, and the 4×4 influence coefficient matrix

is reduced to a 2×2 matrix. The elements of the reduced influence coefficient matrix can be expressed by the following equations, Eqs. A.2– A.5, where $V(i, j)$ is the velocity induced on control point i due to horseshoe vortex j .

$$\mathbf{I}(1, 1) = V(1, 1) + V(1, 1') = (u_{11} + u_{11'}, v_{11} - v_{1'1}, w_{11} + w_{11'}) \quad (\text{A.2})$$

$$\mathbf{I}(1, 2) = V(1, 2) + V(1, 2') = (u_{12} + u_{12'}, v_{12} - v_{1'2}, w_{12} + w_{12'}) \quad (\text{A.3})$$

$$\mathbf{I}(2, 1) = V(2, 1) + V(2, 1') = (u_{21} + u_{21'}, v_{21} - v_{2'1}, w_{21} + w_{21'}) \quad (\text{A.4})$$

$$\mathbf{I}(2, 2) = V(2, 2) + V(2, 2') = (u_{22} + u_{22'}, v_{22} - v_{2'2}, w_{22} + w_{22'}) \quad (\text{A.5})$$

This use of lateral symmetry can easily be expanded to a formation of wings, and the reduction in computation time can be quite significant.

For the case of the wing formation in ground effect, symmetry about the ground plane can be used to further reduce the computation time. Ground effect is simulated by modeling a mirror image of the formation under the $x - y$ plane, and the same method as presented for the case of lateral symmetry can be used to take advantage of the symmetry created about the ground plane. For example, consider a simple two-wing formation in ground effect, at a ground clearance of h , as seen in Fig. A.2.

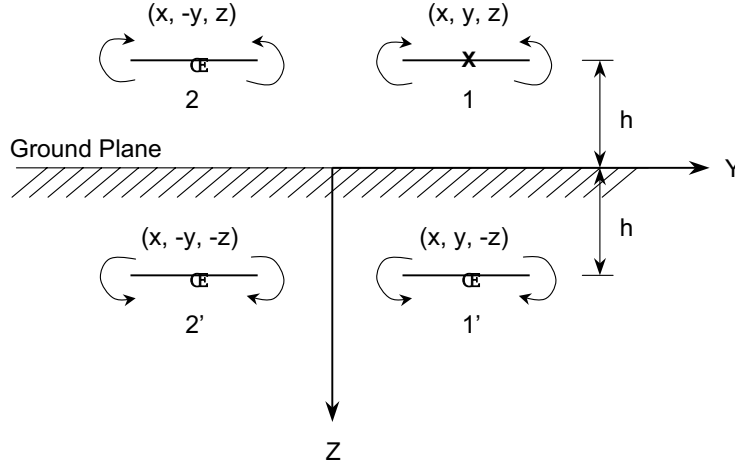


Figure A.2: Two-wing formation in ground effect, with each wing modeled with a single horseshoe vortex.

In this illustration, the vorticity distribution along each wing is modeled with a single horseshoe vortex, and therefore there is a total of four horseshoe vortices. For the purpose of demonstration, consider the induced downwash at control point 1, located at (x, y, z) , due to the velocity induced by horseshoe vortices 1 and 2, and the mirrored horseshoe vortices 1' and 2'. Due to the lateral symmetry, the image horseshoe vortex 2 has the same strength as horseshoe vortex 1, and as demonstrated before, the velocity induced by horseshoe vortex 2 on control point 1, can be evaluated by determining the influence of the actual vortex at a reflected control point located at $(x, -y, z)$. Due to the symmetry about the ground plane, the influence of horseshoe vortex 1' on control point 1, can be evaluated by calling the influence of the actual vortex at point $(x, y, -z)$. And due to both lateral symmetry and symmetry about the ground plane, the influence of horseshoe vortex 2' on control point 1, can be evaluated at point $(x, -y, -z)$. By the inclusion of lateral symmetry and symmetry about the ground plane, the influence coefficient matrix is reduced from a 4×4 matrix to a 1×1 matrix, reducing the computation

time to one-sixteenths. The single element in the reduced influence coefficient can be expressed by the following equation, where again $V_{i,j}$ is the velocity induced on control point i by horseshoe vortex j .

$$\begin{aligned}
\mathbf{I}(1, 1) &= V(1, 1) + V(1, 2) + V(1, 1') + V(1, 2') \\
&= (u_{11} + u_{12} + u_{11'} + u_{12'}, v_{11} + v_{12} + v_{11'} + v_{12'}, \\
&\quad w_{11} + w_{12} + w_{11'} + w_{12'})
\end{aligned} \tag{A.6}$$

When determining optimum lift distributions for a formation of wings in ground effect, using both lateral symmetry and the symmetry about the ground plane, the computational time can be reduced to one-sixteenths. This method has resulted in significant computational savings in the current work when examining large wing formations in and out of ground effect.